Supplementary Materials: Northward Expansion of High-Stature Vegetation Reveals Net Surface-Cooling Feedbacks in the Majority of Canadian Boreal-Tundra Ecozones

Daniel Chukwuemeka Amaogu[1*], Enoch Ofosu[2], Kevin Bradley Dsouza[2], Jérôme Pigeon[1], Lukas U. Arenson[1,3], Richard Boudreault[1,2,4], Juan Moreno-Cruz[5], Yuri Leonenko[2], Pooneh Maghoul[1,6,7*]

[1*]Sustainable Infrastructure and Geoengineering Lab (SIGLab), Department of Civil, Geological and Mining Engineering, Polytechnique Montréal, Montreal, Canada.

[2]Department of Earth and Environmental Sciences, University of Waterloo, Waterloo, Canada.

[3]BGC Engineering Inc., Vancouver, Canada.

[4]Université de Sherbrooke, Sherbrooke, Canada.

[5]School of Environment, Enterprise and Development, University of Waterloo, Waterloo, Canada.

[6]United Nations University, UNU-INWEH, Richmond Hill, Canada.

[7]Centre d'études nordiques, Québec City, Canada.

*Corresponding author(s). E-mail(s): daniel-chukwuemeka.amaogu@etud.polymtl.ca; pooneh.maghoul@polymtl.ca;

1 Introduction

In this supplementary, we provide technical and methodological details that support the overall context, results, and discussion presented in the main paper. These include explicit descriptions of study area, data preprocessing, compositing algorithms, quality metrics, and other analytical steps. Each section presents one methodological component under headings corresponding to those referenced in the main paper.

2 Description of Study Area

The Canadian Boreal Tundra (CBT) study area considered in this study spans about 600 million hectares (5.89 million km^2, Table 1), across which roughly 6.54 billion pixels were analyzed (30 m resolution). Out of the 5.89M km^2, about 420.13km^2 are covered by water bodies. The CBT area analyzed in this study covers nine Canadian ecozones (Table 1), including the Taiga Shield (TS), Taiga Shield West (TSW), Boreal Sheild (BS), Boreal Cordillera (BC) Taiga Cordillera (TC), Taiga Plains (TP), Tundra Cordillera (TUCO) Hudson Plains (HP), and Southern Arctic (SA) [1–6]. Disturbances such as wildfire, pest, and disease outbreaks, occurring at variable return intervals, are part of the natural cycle of the CBT system. Elevation ranges from –252 m above sea level (ASL, Figure1 Panel A) in low-lying plains to over 4400 m ASL in the Boreal Cordillera, influencing both vegetation distribution and density. The dominant species across the ecozones are largely *Picea* spp (Figure1 Panel C). Full disturbance regimes, management histories, and floristic conditions across these regions have been detailed by [1, 2, 4, 7–9] and are pictorially illustrated in Figure 1.

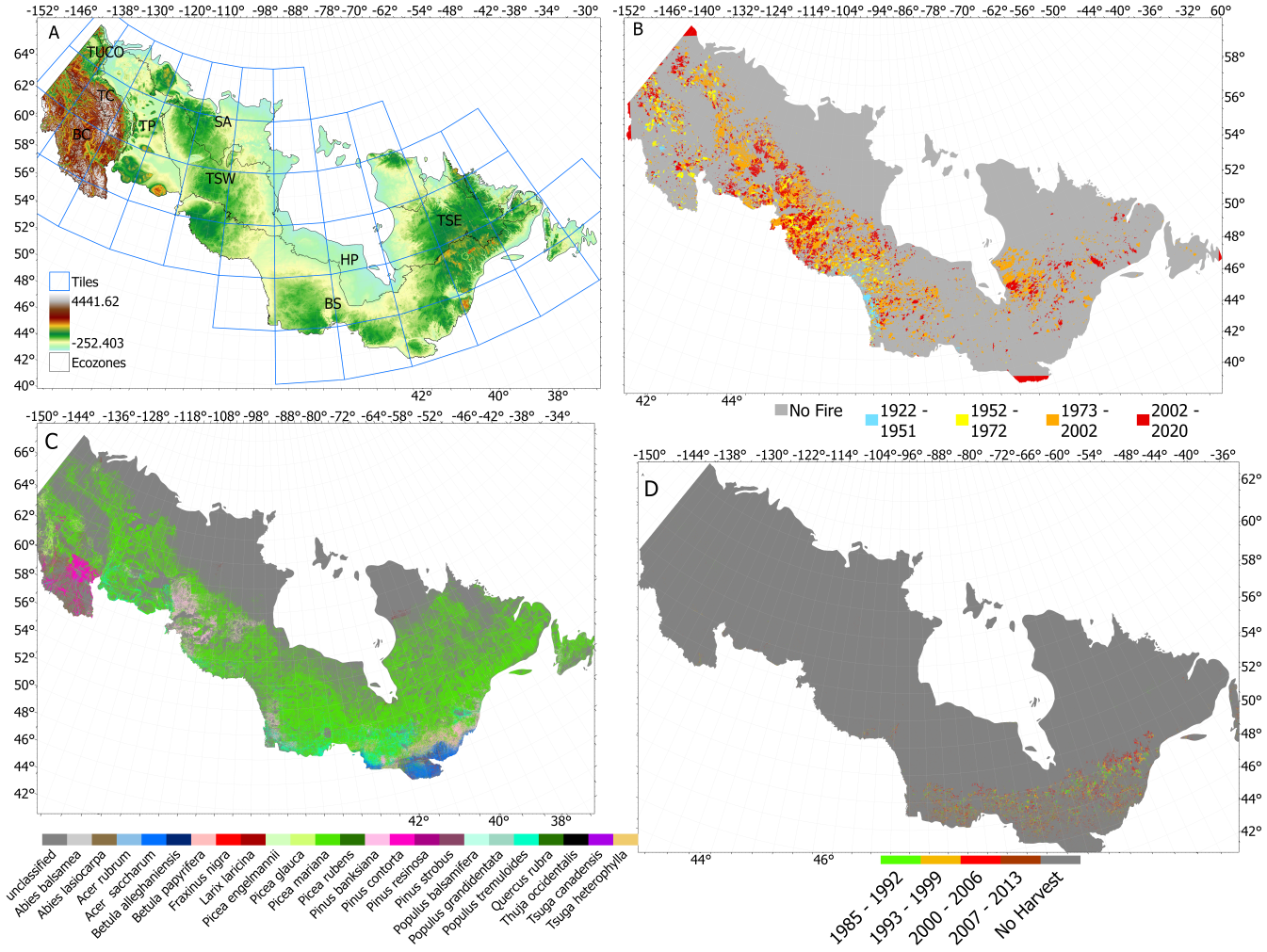


Fig. 1: Ecological and topographical description of the study area. Panel A shows elevation distribution across the ecological zones with the tiling system used in this study. Panel B and D are the distributions pixels where wildfire and harvest occured between 1986 and 2022 while panels C is the dominant 1984 tree species distribution within each pixel point of the study area. Maps were generated using ArcGIS Pro.

Table 1: Estimated treed vegetated areas across selected Canadian Boreal–Tundra (CBT) ecozones.

Ecozone	**Ecozone Area** (10^3 (km^2))	**Water Bodies** (10^3 (km^2))
Southern Arctic	949.45	57.60
Taiga Plains	554.07	64.65
Boreal Shield	1893.42	155.82
Boreal Cordillera	557.97	8.86
Taiga Cordillera	231.15	1.30
Hudson Plains	349.81	4.26
Taiga Shield East	702.38	55.25
Tundra Cordillera	28.99	0.01
Taiga Shield West	619.11	72.38
Total	**5886.35**	**420.13**

3 Geodesic Pixel Area Estimation

In all places in the main paper and supplementary where we explicitly mention that area was estimated by the geodesic approach, we mean that pixel counts were converted to true surface area on the sphere rather than using a planar approximation. This was applied in two complementary ways, depending on whether zones were defined as latitude

bands or as ecozones. **(i) Latitude-band basis.** When zones were defined as 1° latitude bands, the surface area of each 0.1° × 0.1° raster cell was computed geodesically using the spherical formula

$$A \;=\; R^2\,\Delta\lambda\,\big(\sin\varphi_2 - \sin\varphi_1\big),$$

where $R = 6{,}371{,}008.8\,\mathrm{m}$ is Earth's mean radius, $\Delta\lambda$ is the longitudinal width of the cell in radians, and φ_1, φ_2 are the southern and northern edges of the band. A single midpoint latitude (e.g., 44.5° for the 44–45N band) was taken as representative of the band, and the resulting per-pixel area was multiplied by the number of valid pixels to obtain valid surface area in m^2 and km^2. **(ii) Ecozone basis.** When zones were defined as ecozone polygons (irregular and spanning multiple latitudes), we instead computed pixel areas row by row across the raster. In this case, the area of a single pixel centered at latitude φ was evaluated as

$$A(\varphi) \;=\; R^2\,\Delta\lambda\,\Big[\sin\big(\varphi + \tfrac{\Delta\varphi}{2}\big) - \sin\big(\varphi - \tfrac{\Delta\varphi}{2}\big)\Big],$$

where $R = 6{,}371{,}008.8\,\mathrm{m}$, and $\Delta\varphi$ and $\Delta\lambda$ are the cell dimensions in radians. This produced a vector of per-row pixel areas that naturally shrink toward the poles. Valid area for each ecozone was then obtained by summing over the rows where the zone mask was true. By applying the geodesic correction in both contexts, we ensured that all reported areas are unbiased by latitude, which is critical in high-latitude domains such as the Canadian Boreal Tundra.

4 BAP NDVI Annual Compositing Algorithm Implementation

In this study we adopted a modified best available pixel (BAP) algorithm to composite the peak annual normalized difference vegetation index (NDVI) time series (June – September [10–12]) between 1986 and 2023 from Landsat 5, 7–9 image scenes. our BAP implementation was within the Google Earth Engine (GEE) Platform. The core principle of BAP is that it treats each NDVI pixel within a collection of the same scenes over a year individually, evaluates its quality, and selects the pixel with the highest quality score to populate the composite grid. In this study, we calculated four component scores for each Landsat acquisition within the n-year collection: the sensor score, the day-of-year (DOY) score, the distance-to-cloud (cloud-shadow) score, and the opacity score as follows:

4.1 Sensor score

We derive the sensor score (Equation1) by assigning a value of 1.0 to all pixels from Landsat 5, 8, 9 and pre–June 1 2003 Landsat 7 ETM+ acquisitions, and a penalty score of 0.5 to all post–June 1 2003 ETM+ scenes to account for SLC-Off data gaps.

$$S_{\text{sensor}} = \begin{cases} 1.0, & \text{for Landsat 5, 8, 9, and pre–June 1, 2003 Landsat 7 ETM}^{+}\text{ acquisitions,} \\ 0.5, & \text{for post–June 1, 2003 Landsat 7 ETM}^{+}\text{ acquisitions (SLC-Off period).} \end{cases} \tag{1}$$

4.2 DOY Score

Next, we calculated the DOY score for each pixel in the n-year collection following Griffiths *et al.* [13]:

$$\text{Score}_{\text{DOY},i,k} = \frac{1}{\sigma\sqrt{2\pi}} \exp\left(-\tfrac{1}{2}\left(\frac{\text{DOY}_{i,k}-\mu}{\sigma}\right)^2\right) \tag{2}$$

where $\text{DOY}_{i,k}$ is the day-of-year of the kth acquisition at pixel i, $\mu = 213\,\text{days}$ (August 1 when vegetation is most developed), and $\sigma = 38\,\text{days}$ (roughly corresponds to ±5-6 weeks around the midpoint). This sets the DOY-213 (August 1) NDVI observation to a maximum score of 1, with the score then decaying symmetrically according to a Gaussian curve ($\sigma = 38\,\text{days}$) so that acquisitions farther from peak leaf-area development receive progressively lower weights.

4.3 Cloud Distance Score

The next quality metric, the distance-to-cloud score, quantifies how far each clear-sky NDVI pixel in the n-year collection lies from any flagged cloud or shadow. We first use the QA (quality assurance) band (bit 3 for clouds, bit

4 for shadows) to build a binary mask M_{cloud}, then compute for each remaining n-year NDVI pixel i its Euclidean distance to the nearest masked pixel [13, 14]:

$$D_i = \sqrt{D_T\big(M_{\text{cloud}}(i)\big)} \tag{3}$$

where $D_T(M_{\text{cloud}})$ is the squared-distance transform of the cloud-shadow mask. We then capped each distance at 50 pixels as the maximum possible value

$$D_{\text{clamp},i} = \min\big(D_i,\, 50\big) \tag{4}$$

and map the capped value into a continuous score between 0 and 1 via a logistic function centered at 25 pixels [13, 14]:

$$\text{Score}_{\text{CloudDist},i} = \frac{1}{1 + \exp\big[-0.2\,(D_{\text{clamp},i} - 25)\big]} \tag{5}$$

4.4 Opacity Score

The next computed quality metric was the opacity score, which quantifies atmospheric clarity for each NDVI pixel in the n-year Landsat scene collections. For each scene, we converted the aerosol bands into an aerosol optical thickness AOT_i and then remapped that value into a 0–1 weight. Specifically, for Landsat 5 and 7 we extracted the `SR_ATMOS_OPACITY` band and multiplied by 0.001 to obtain AOT_i, whereas for Landsat 8 and 9 we extracted bits 7–8 of `SR_QA_AEROSOL` and rescaled the resulting integers $\{0, 1, 2, 3\}$ to $\{0.05, 0.10, 0.20, 0.30\}$. We then defined a clear-sky cutoff $O_{\min} = 0.2$ and a hazy-sky cutoff $O_{\max} = 0.3$ (midpoint $O_{\text{mid}} = 0.25$). NDVI pixels with $\text{AOT}_i \le O_{\min}$ received full weight (score = 1), those with $\text{AOT}_i \ge O_{\max}$ received zero weight, and intermediate values were mapped smoothly via the inverted logistic function [13, 14]:

$$\text{Score}_{\text{Opacity},i} = 1 \;-\; \frac{1}{1 + \exp\big[-4\,\big(\min(\text{AOT}_i, O_{\max}) - O_{\text{mid}}\big)\big]} \tag{6}$$

This ensures that the clearest (low-AOT) observations carry maximum weight, the haziest (high-AOT) observations are fully penalized, and intermediate aerosol loads receive progressively lower weights in the TotalScore.

4.5 Total Quality Score

Finally, for each year in our n-year NDVI scene collection, we selected, at every 30 m grid cell, the single NDVI pixel with the highest total quality score. The scoring functions inherently weighted each quality component toward the final total value. For example, recall that the Gaussian day-of-year function (Equation 2) emphasized acquisitions near the regional peak of vegetation activity, while the logistic distance function (Equation 5) reduced the contribution of pixels located close to clouds or shadows. Similarly, the inverted logistic opacity function (Equation 6) lowered the influence of scenes with high aerosol optical thickness, and the sensor penalty reduced the weight of Landsat 7 SLC-off acquisitions. Together, these nonlinear scoring functions acted as implicit weighting that prioritized pixels with optimal temporal, radiometric, and geometric conditions for compositing, ensuring that the clearest and most representative observations received the highest summed quality scores. We then used these best-pixel selections, drawn from different scenes within each year, to populate the composite grid, yielding a continuous 38-year (1986–2023) time series of annual peak-season NDVI mosaics.

5 NDVI Ensemble Trend Fitting

NDVI, despite its known saturation issues, has remained the most widely used vegetation spectral index for detecting areas of vegetation change since its introduction in 1973 [15]. In addition, its strong coupling with land cover, vegetation structure and bio-geophysical properties makes it a high-value, yet computationally efficient, metric for not only detecting changes but also provides opportunity for empirically and physically deriving the drivers of, and feedback associated with detected vegetation-surface changes. For example, NDVI correlates strongly with temperature [16, 17]), mass movements (e.g., erosion, landslides [18]), evapotranspiration [17], carbon [19] and surface energy balance [20]. NDVI has also been used for the characterization of land cover [21], vegetation phenology and structural metrics like leaf area index (LAI), plant functional types (PFTs) [22–24], which are key parameters in state of the art Earth-system land surface models (LSMs) [25]. Therefore, by leveraging known NDVI value ranges for land-cover and PFT classes (bare ground ≈ 0.01; water ≈ 0; shrubs ≈ 0.3; evergreen forest ≈ 0.7 [26–28]) and anchoring each pixel's trend distribution to its apriori baseline class, one could predict its probable end-state cover type over the analysis

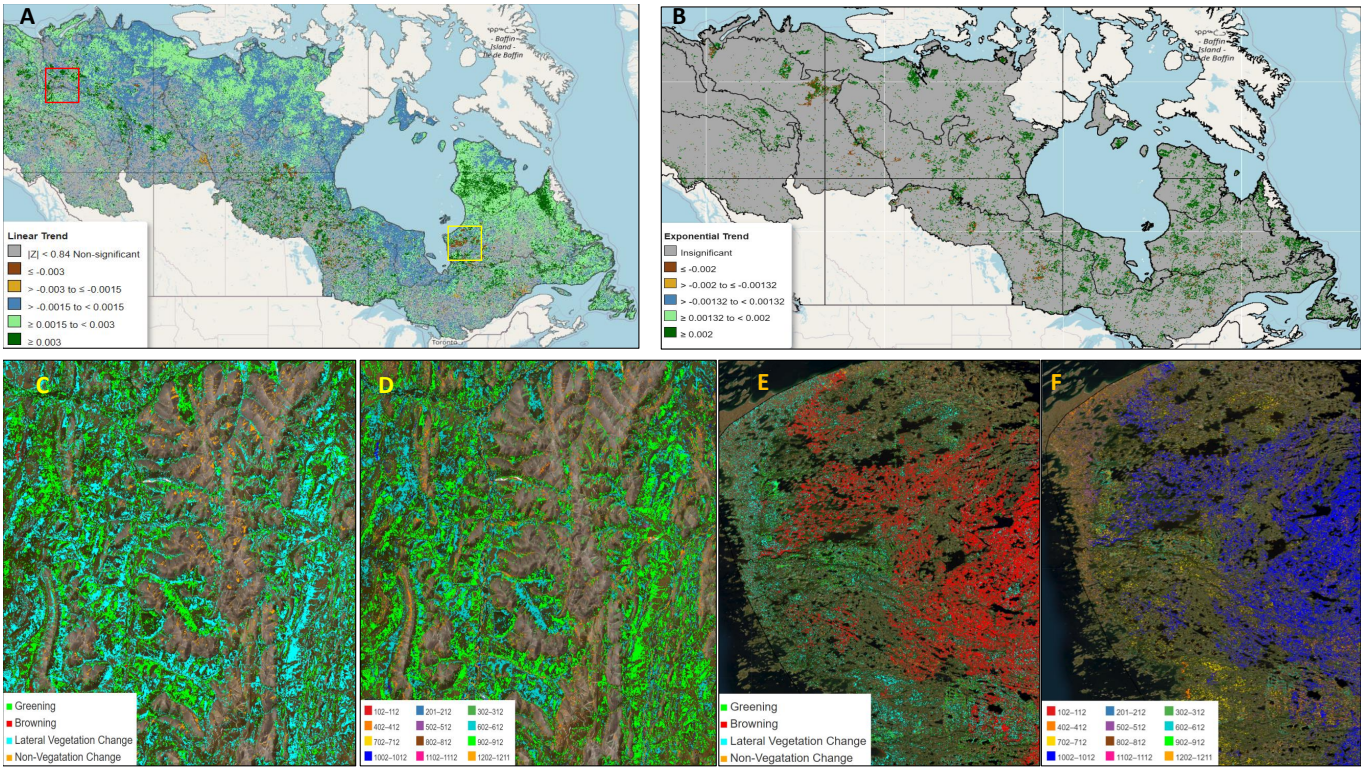


Fig. 2: Spatial distribution of NDVI trend and land cover transition. Panel A is the NDVI trend derived from Theil-son and Kendal test, Panel B is showing trend fitted by the exponential function. Panel C and E is the snippet of landcover ecological class transition of the red and yellow bounding boxes in Panel A and D and F are the actual landcover class transition driving the observed changes. Background basemap in Panels A to F: OpenStreetMap Style © OpenStreetMap contributors, Microsoft, Esri Community Maps contributors; rendered via Esri in ArcGIS Pro

period. Moreover, by noting the points and periods at which pixels shift between PFT or land-cover categories (for example, from shrubland into young forest), we can attribute spectral greening and browning to vegetation-change dynamics and identify natural vegetation transition analogues in the CBT for further analysis of vegetation-driven surface energy and ecosystem responses.

5.1 Why Ensemble Trend Fitting Was Adopted in This Study

Vegetation change across the CBT is rarely linear. Successional recovery, shrub expansion, and post-disturbance regrowth often follow nonlinear paths that simple monotonic models cannot capture. To address this, we implemented an ensemble NDVI trend fitting framework at 30 m resolution, integrating linear, exponential, logarithmic, and logistic models within Google Earth Engine (GEE) despite its nonlinear fitting limitations. Each pixel's 1986–2023 time series was fitted sequentially: first with a linear model; then, for statistically significant linear fits, we tested under- and overestimation by applying nonlinear alternatives; and finally, for pixels remaining non-significant, exponential and logistic models were applied to recover overlooked dynamics. This structured sequence allowed us to recover many pixels that would have been misclassified as "no trend" by linear-only methods (Figures 3 and 2 Panels A and B), revealing consistent NDVI increases (≥ 0.0001 yr^{-1}) across ecozones, with 5% showing exponential greening (2 Panels B). Further post-analysis showed that the logistic models captured less than 30 pixels in the vegetated areas, and this warranted us to limit our further analsysis with only the linear and exponential derived vegetation trend grids.

We adopted ensemble fitting because classical linear approaches (e.g., Theil–Sen or linear regression, Figure 3) risk underestimating trend magnitudes or masking nonlinear hotspots. By contrast, our ensemble isolates pixel-level tipping points, bridging a major gap left by kilometer-scale pan-Arctic analyses that smooth over local heterogeneity. Ultimately, by adopting this ensemble NDVI framework, we provided a stronger foundation for linking spectral signals with land cover, PFT shifts, and biogeophysical feedbacks [29–32]. This approach allowed us to expose cases where linearity assumptions produced artifacts, identify hotspots of nonlinear dynamics, and support interpretation of vegetation-driven feedbacks that raise permafrost thaw and thermokarst risks. By filling this methodological gap, we ensured that the trajectories presented in the main paper rest on a comprehensive and technically robust foundation.

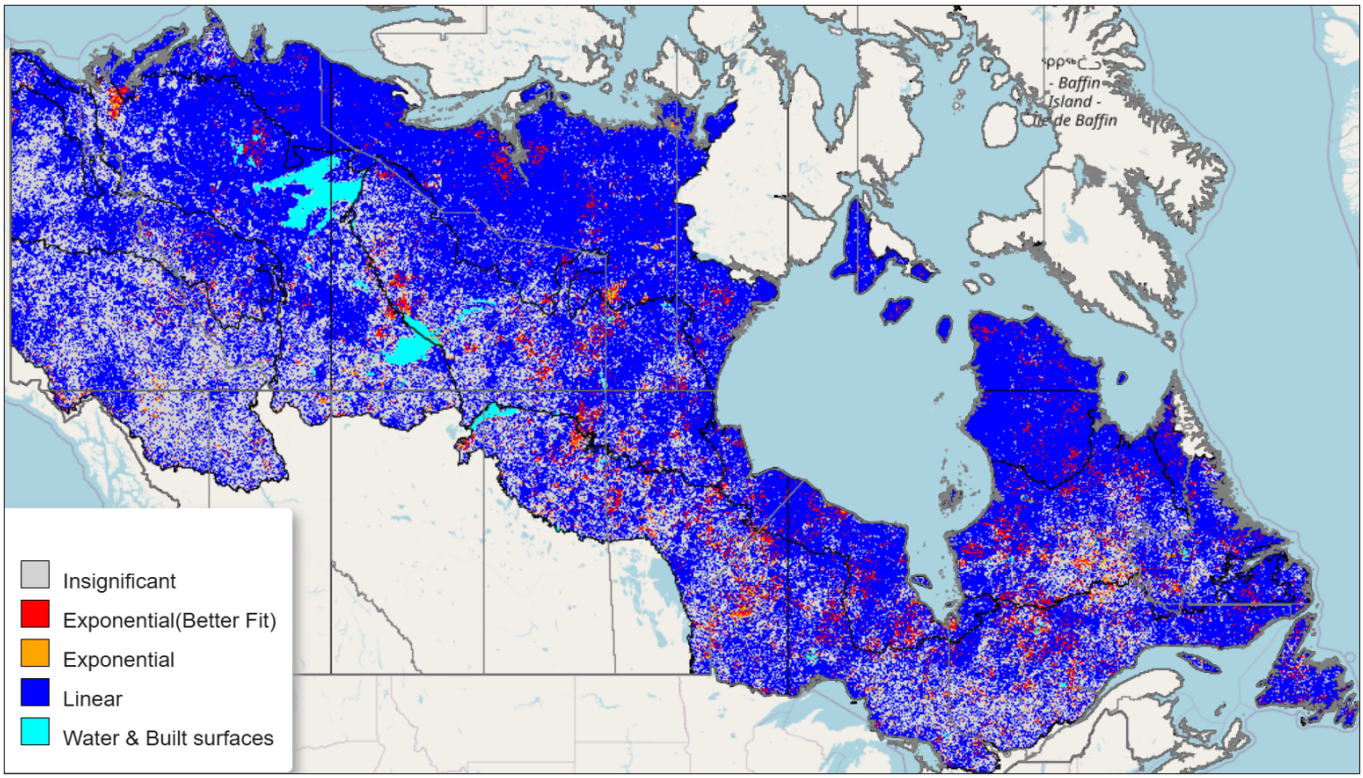


Fig. 3: Spatial proportion of linear and exponential NDVI trends. Red patches mark pixels where the Theil–Sen linear fit underestimated the NDVI trend but an exponential model provided a better fit; gold patches mark pixels where an exponential trend was recovered from pixels initially classified as non-significant by Theil–Sen. Blue are all linear trends pixels and gray captures all insignificant pixels. Background basemap: OpenStreetMap Style (© OpenStreetMap contributors, Microsoft, Esri Community Maps contributors; rendered via Esri ArcGIS Pro

A key limitation introduced by using GEE to fit our exponential trend through log–linear transformations is that the starting NDVI value must be non-negative, and this holds the same in our theoretical NDVI-driven land cover transition Monte Carlo simulations. This means that the reported ∼5% exponential greening only accounted for actual changes occurring where land cover had at least NDVI ≥ 0.1, in our context likely vegetated barelands or early shrub cover.

Table 2: Landsat revisit statistics for peak-season acquisitions (July 1–Sept 30).

Period	Sensors available	Revisit (days)	Max pixel obs.
1986–1999	Landsat 5 (TM)	16	4
1999–2013	Landsat 5 (TM), 7 (ETM$^+$)	8	8–9
2013–2021	Landsat 7 (ETM$^+$), 8 (OLI/TIRS)	8	8–9
2021–2023	Landsat 7 (ETM$^+$), 8 (OLI/TIRS), 9 (OLI-2/TIRS-2)	4	13

5.2 Ecozone-Level NDVI Trends and Threshold Exceedance

From our comprehensive review, it became clear to us that the terms greening and spectral greening are often used interchangeably, with little distinction [29]. Evidence for how well satellite-derived vegetation indices capture actual vegetation change on the ground remains inconsistent [33–36]. Reported NDVI trends frequently diverge across satellite datasets [12, 37], and no single sensor–index pairing provides a consistently reliable match with in-situ observations [33]. Moreover, we found no benchmark in the literature that indicates when a spectral greening trend should have a high likelihood of producing a land cover shift within a given timeframe. In practice, Arctic spectral greening assessments, whether describing vegetation intensification, northward invasion, or shrubification remain blurry, as they typically reduce all non-zero positive NDVI trends to greening and all non-zero negative trends to browning. Our

contribution in this paper is to move beyond this simplification by attempting, through NDVI trend thresholding, to link spectral Arctic greening to actual land cover shifts (greening or browning), and by specifying theoretically validated benchmarks within which NDVI spectral trends can serve as a guide for projecting endpoint vegetation conditions from historical baselines. This was the motivation for implementing our Monte Carlo NDVI-driven land cover simulations. Through this approach, we provide threshold ranges (Table 3) of NDVI trend values over the 38-year period that can be ascribed to greening or browning in the context of their capacity to nudge land cover from one type or density class into another.

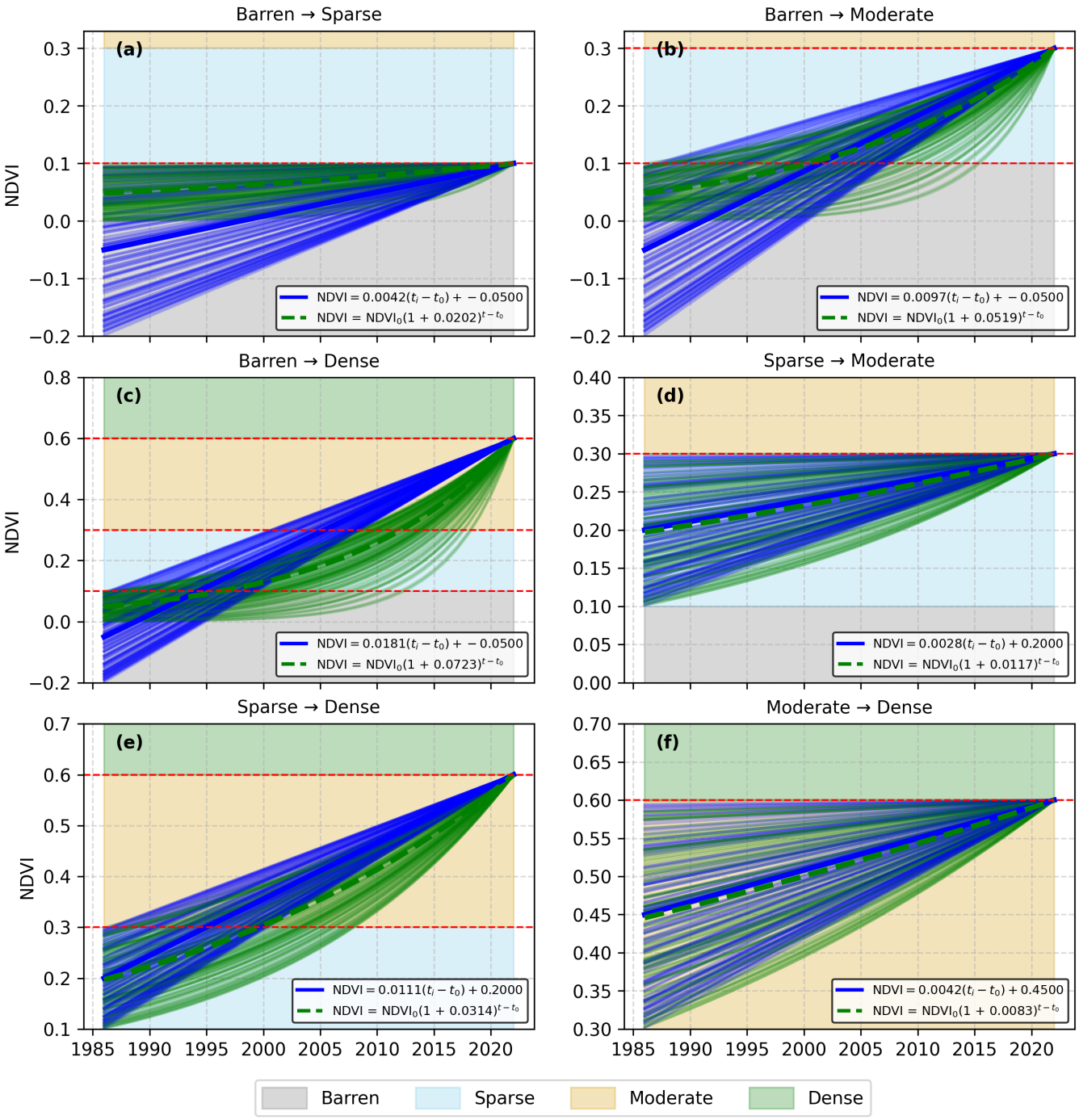


Fig. 4: Monte Carlo-simulated NDVI trajectories used to estimate the trend thresholds required for land-cover transitions during 1986–2022 from: (a) barren to sparse,(b) barren to moderate, (c) barren to dense, (d) sparse to moderate, (e) sparse to dense, and (f) moderate to dense vegetation cover. In panels (a)–(f), linear trajectories are shown in blue, while exponential trajectories are shown in green. Thin lines represent individual simulations, whereas the thick solid blue and thick dashed green lines represent the median linear and exponential trajectories, respectively. The corresponding median trend equations are presented in the inset of each panel. Horizontal red dashed lines indicate the NDVI thresholds separating the barren, sparse, moderate, and dense vegetation-cover classes, represented by grey, light blue, beige, and green backgrounds, respectively.

6 Land Cover Transition Analysis

6.1 Description of landcover datasets

Two landcover datasets were employed in this study for analysis, including the Canadian annual landcover datasets from Virtual Land Cover Engine (VLCE2) [38] between 1984 to 2022 and the global landcover dataset of 1985 to 2022 (GLC_FCS330D, hereafter GLFC V3) [39]. Canadian-VCLE2 generated by the Composite2Change (C2C) algorithm provides annual 30 m landcover maps for Canada (1984–2022) excluding parts of the Southern Arctic. C2C integrates Landsat BAP composites with ancillary lidar, hydrology, topography, and historical landcover data, achieving an overall accuracy of 77.9% [38]. Canadian-VCLE2 landcover classes include water, snow/ice, rock/rubble, exposed/barren, bryoids, shrubs, wetland (treed and non-treed), herbs, coniferous, broadleaf, and mixedwood. In contrast, GLFC v3 provides semi-annual global 30 m landcover maps (1985–2022), generated via change detection, adaptive updates, and spatiotemporal optimization (80.9% accuracy from 84,000 samples) [39]. Though from 1985–2000, GLFC was updated every five years, with each epoch based on multi-year imagery for classification stability [39].

6.2 Landcover transition quantification

In the main paper, we reported land cover change dynamics across the CBT from 1986 to 2022 by implementing a land cover transition matrix algorithm on the two datasets described above. In practice, the Google Earth Engine landcover transition algorithm we developed sequentially examined stacks of the unified annual landcover datasets. For each year, it produced rasters whose coded pixel values denoted the specific FROM-TO transition (e.g., forest to shrubland). A simple FROM-TO coding scheme was used, where each transition was defined as $(\text{FROM} \times 100) + \text{TO}$, with FROM representing the baseline class and TO the class in the target year (e.g., Shrubs (6) to Coniferous (10) = 610). The coded raster values correspond to those shown in Figure 5. Because the unified annual Canadian-VCLE2 and GLFC V3 landcover time series spans 1985 to 2022, the first transitions appear from 1986, resulting in 37 yearly transition rasters across a 37-year series.

To ensure that these transition results could be trusted when declaring the final pixel end state in 2022, we introduced the concept of "meaningful ecological change." We defined this as a 2022 landcover type annual-derived transition raster pixel whose 2022 transition class matched its 2020 or 2021 state (signifying transition completion) and that had followed a consistent ecological successional trajectory since its first change within the 37-year series. The 2022 landcover transition pixels that met the 2020/2021 persistence condition were then subjected to an additional filtering step: verifying whether the sequence of their changes represented a consistent ecological progression toward the 2022 endpoint. For this, we computed the total number of times within the 36 annual landcover transition stack that each pixel underwent changes consistent with its 2022 landcover type transition class.

For example, if a landcover pixel's transition end state in 2022 was mixedwood, then an ecologically consistent trajectory would typically involve passing through shrub, broadleaf, and coniferous stages before reaching mixedwood, and vice versa for the reverse sequence. While such stepwise progressions may not always occur in reality, since trees can sometimes colonize new ground rapidly, it is also true that the early stages of such colonization would almost certainly be spectrally detected as herb or shrub cover. Recognizing this, we computed meaningful ecological change through a modified transition algorithm, which was set to true when the number of times within the 37 transition years that ecologically consistent transitions occurred was higher than inconsistent ones. The 2022 landcover transition pixels that failed this test were, in our study, treated as stable relative to their 1986 baseline. In effect, our analysis assumed that large abrupt jumps from one landcover class to another should not occur within the final years of the series (2021–2022). Although such abrupt changes are possible, they are unlikely to be widespread in the CBT. This filtering step primarily addressed the issue of pixel spectral flipping, which can arise in landcover products that are derived predominantly (though augmented by other covariates) from optically sensed datasets.

6.2.1 Landcover transition classification: Greening, Browning, Stable

Given the quality control we applied in deriving the final 2022 land cover transition raster, we used its values to generate the three results presented in Table 1 and Figures 3–4 of the main paper. We define the "land cover transition from classes" raster, referenced in the NDVI–land cover change cross-validation (Table 1, main paper), as the final refined land cover transition layer derived from the annual land cover time series up to 2022. We intersected this layer with randomly drawn pixel samples from the upper (classes 5–4) and lower (classes 1–2) of NDVI-derived greening and browning categories (Table 3; see also Methods Section 4.4–4.6) to assess the correspondence between NDVI-derived vegetation changes and land cover transitions derived from an independent annual land cover time series dataset.This final 2022 raster contains values categorized as vegetation loss (browning), gain (greening), stable (no change) among

others, as illustrated in Figures 5 and 2 Panel D and F. It is this raster's pixels (Figure 2), containing such values (from 101 to 1212), that we interpreted as greening and browning and intersected with the NDVI-derived greening and browning classes (Table 3 and Figure 2 Panel C and E) to inform our spectral trend and landcover trend correlation presented in Figures 3-4 (main paper).

For example, the value "410" in the derived " 2022 landcover raster" is termed greening, because it shows that landcover moved from barren land in 1986 to coniferous forest in 2022 (i.e., greening). Also value such as "1009" means transition from coniferous to herbs (browning) between 1986 to 2022. Also "1212" is interpreted as stable since no transition occured (i.e., in 1986 landcover was mixedwood and it remained so until 2022). Therefore when each of greening landcover transition pixel (e.g 410) intersects correctly with the NDVI trend reclassified raster containing classes 4 or 5 (greening, Table 3), it is termed a greening correct match (True Positive). Likewise, if land-cover transition browning classes (e.g "1009", "1209" etc) intersects with the NDVI trend reclassified raster containing classes 1 or 2 (browning), it is termed a browning correct match (True Positive)

To summarize these results obtained from GEE per ecozone and latitude and derive the Figures we presented in this study, we post-processed them in ArcGISPro and GEE-python api. We used ArcGISPro to first divide the ecozone polygons by 1-degree latitudinal bands into 27 bands. We then used both the ecozone polygons and the latitudinally divided ecozone polygons individually, each serving as a Zone field. Through the ArcGISPro Tabulate Area function and its Python extension, we geodesically computed the area of the refined final 2022 landcover type transition raster values across the two zone fields (latitude bands and ecozones). This enabled us to derive the results presented in the above-mentioned figures and tables.

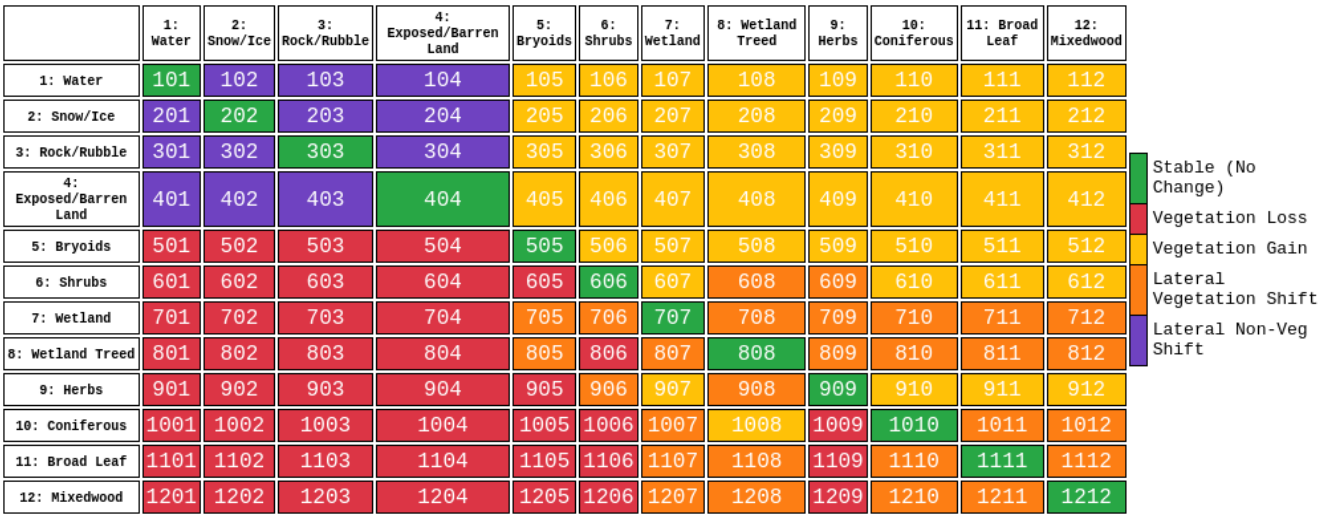


Fig. 5: Landcover transition matrix

Table 3: Lookup Values for NDVI slope reclassification (linear vs. exponential trends)

Class	Description	Linear slope (NDVI yr^{-1})	Exponential slope (NDVI yr^{-1})
1	Significant browning	≤ -0.003	≤ -0.002
2	Moderate browning	$-0.003 <$ slope ≤ -0.0015	$-0.002 <$ slope ≤ -0.00132
3	Statistically stable	$-0.0015 <$ slope < 0.0015	$-0.00132 <$ slope < 0.00132
4	Moderate greening	$0.0015 \leq$ slope < 0.003	$0.00132 \leq$ slope < 0.002
5	Significant greening	≥ 0.003	≥ 0.002

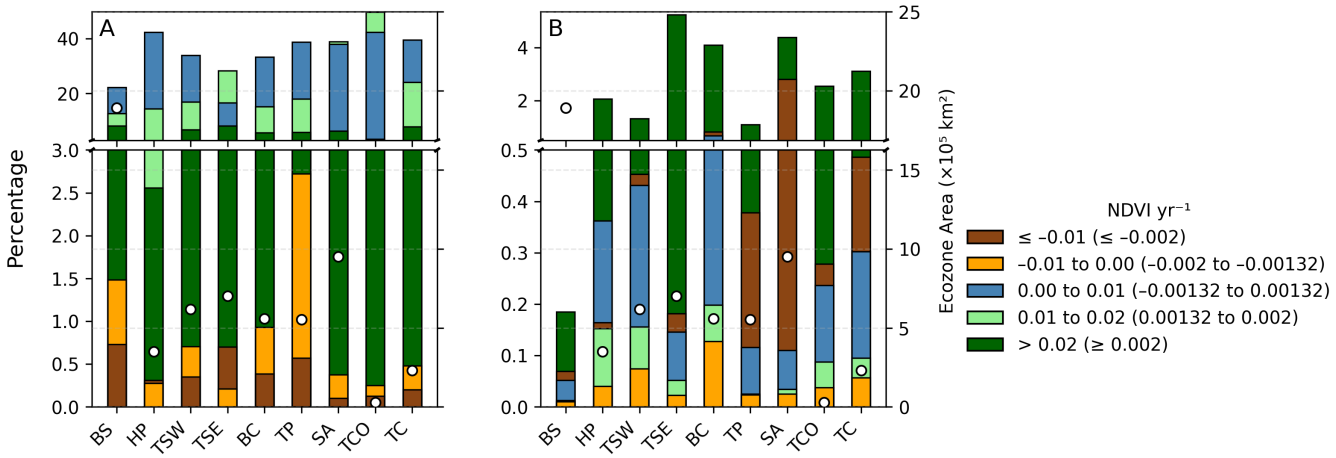


Fig. 6: Relative NDVI trend-class area by ecozone. Panels (a) and (b) show, for each ecozone, the percentage of area falling into each NDVI trend bin from the linear and exponential NDVI trends, respectively. Percentages are computed relative to each ecozone's total area. Within each ecozone, NDVI trend classes are visually layered from lower to higher percentage contribution to preserve the visibility of low-area trend categories, while each colored segment represents the absolute percentage contribution of its corresponding NDVI trend class. In the legend, labels outside parentheses refer to linear bins; labels inside parentheses refer to exponential bins. Dots mark ecozone area (km^2), plotted against the right-hand (secondary) y-axis.

Table 4: Initial class area (1986) by ecozone. Units: 10^3 km^2.

Class	SA	TP	BS	BC	TC	HP	TSW	TUCO	TSE
Bareland	20.37	28.82	24.53	25.95	4.18	40.45	59.70	1.21	38.57
Broadleaf	8.75	14.42	75.56	71.76	1.59	25.48	32.84	1.20	135.90
Bryoid	3.68	12.56	12.02	13.92	10.93	7.28	29.70	2.97	11.03
Coniferous	169.07	185.08	810.89	190.03	21.13	202.60	212.74	2.35	346.87
Herbs	416.51	130.26	285.08	95.55	58.75	158.83	218.77	13.12	188.74
Mixedwood	23.57	3.48	305.00	28.49	5.96	49.84	100.41	0.85	77.94
Shrub	69.86	75.60	169.57	125.37	34.66	120.67	91.75	4.87	185.05
Wetland	225.57	84.60	149.20	60.76	11.67	49.45	87.77	1.80	55.59
Wetland Treed	92.33	16.63	52.39	49.46	11.97	46.77	79.24	0.57	58.44

Notes. Columns are ecozone abbreviations; rows are land-cover classes used in the main text. Values give the 1986 baseline extent for each class and ecozone. See Tables 14–15 for their ecozone-level baseline energy fluxes as at 1986. Ecozone abbreviations: SA = Southern Arctic; TP = Taiga Plains; BS = Boreal Shield; BC = Boreal Cordillera; TC = Taiga Cordillera; HP = Hudson Plains; TSW = Taiga Shield West; TUCO = Tundra Cordillera; TSE = Taiga Shield East.

Table 5: Annualized fractional change in class share (1986–2022) by ecozone. Units: $\times 10^{-3}\,\mathrm{fc\,yr^{-1}}$.

Class	SA	TP	BS	BC	TC	HP	TSW	TUCO	TSE
Bareland	0.10	−0.57	0.12	0.11	0.08	−0.40	0.12	0.49	0.42
Broadleaf	−0.27	0.05	0.50	−0.04	0.02	0.14	−0.40	0.39	0.84
Bryoid	0.02	−0.18	−0.06	0.12	0.04	0.00	0.20	−0.01	−0.60
Coniferous	−0.20	1.17	−1.83	1.29	1.13	2.08	−0.88	0.44	0.19
Herbs	−3.98	−6.43	−3.64	−1.39	−3.13	−1.54	−6.93	−3.28	−6.48
Mixedwood	0.02	0.20	1.29	0.70	0.82	1.17	0.56	0.60	0.31
Shrub	0.40	−0.39	0.14	−0.96	0.61	0.60	0.43	1.85	0.91
Wetland	−0.16	−0.55	−0.31	−0.06	−0.77	−1.54	−0.43	−0.37	−1.79
Wetland Treed	−0.48	0.33	0.23	0.23	0.21	0.99	0.34	0.21	0.44

Notes. Rates are computed per pixel as $(p_{2022} - p_{1986})/36$ and reported as $\times 10^{-3}$ of ecozone fractional cover per year ($\mathrm{fc\,yr^{-1}}$, where $\mathrm{fc} \in [0, 1]$). Positive values indicate gains in class share; negative values indicate losses. For area-change interpretation, multiply the rate by the ecozone area (Table 1) to obtain $\mathrm{km^2\,yr^{-1}}$. SA = Southern Arctic; TP = Taiga Plains; BS = Boreal Shield; BC = Boreal Cordillera; TC = Taiga Cordillera; HP = Hudson Plains; TSW = Taiga Shield West; TUCO = Tundra Cordillera; TSE = Taiga Shield East.

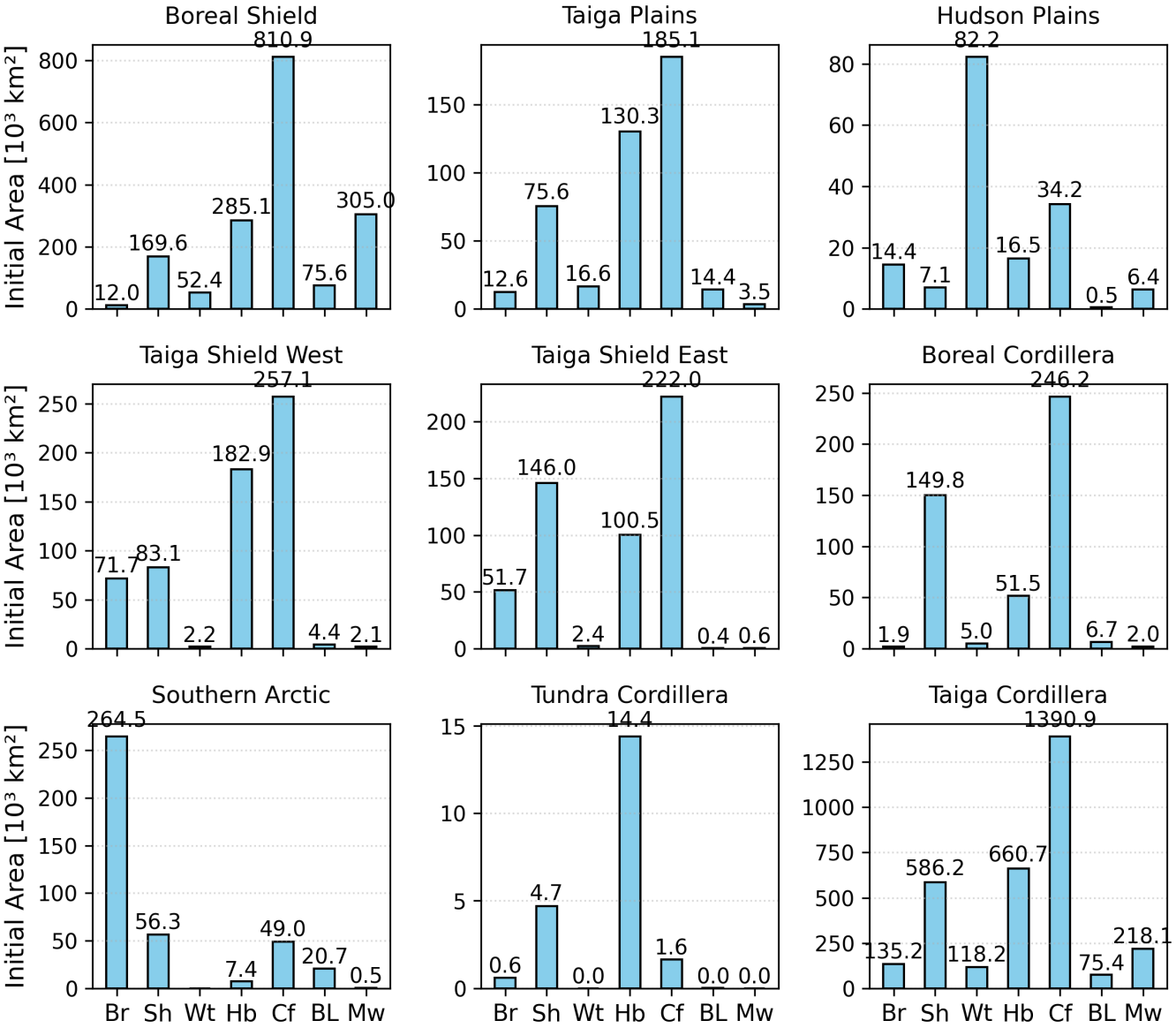


Fig. 7: I986 (Baseline) Landcover of the Ecozones. Area values are computed by geodesic ensuring that pixel conversion to area takes account latitudinal influence. Br= Bryiod, Sh = Shrub, Wt = Wetlland treed, Hb = Herbs, Cf = Conifers, BL = Broadleaf and Mw = Mixedwood

Table 6: Ecozones with net forest change (1986 baseline to final year). Positive values indicate expansion; negative values indicate contraction. Forest = Wetland-treed + Conifer + Broadleaf + Mixedwood. Units: Δ in $\mathrm{k\,km^2}$.

Eco	Trend	Forest (All Trees)		Conifer		Broadleaf		Mixedwood		Wetland-treed		Main Veg. driver
		Δ	%	Δ	%	Δ	%	Δ	%	Δ	%	(Class; Δ / %)
SA	Loss	−8.9	−12.7	−8.54	−17.4	−1.54	−7.4	1.17	146.5	—	—	Shrub offset 13.81 / 24.5
TSW	Loss	−3.5	−3.4	−28.6	−11.1	9.17	208.5	7.37	345.3	—	—	Shrub offset 11.55 / 13.9
TUCO	Gain	1.30	89.3	1.23	72.5	0.02	670.1	0.03	1355.4	0.00	194.7	Conifer; 1.23 / 72.5
HP	Gain	42.03	7.7	−7.18	−21.2	3.93	9.5	+3.93	18.1	45.50	55.3	Wetland-treed; 45.50 / 55.3
TP	Gain	17.79	15.9	23.26	12.6	−0.52	−6.0	−5.02	—	0.01	—	Conifer; 23.26 / 12.6
BCO	Gain	13.80	15.1	17.27	7.0	12.67	209.1	0.25	2.2	−16.39	−4.4	Broadleaf; 12.67 / 209.1
TSE	Gain	8.49	12.5	22.62	10.2	1.03	17.6	−0.45	−2.7	−14.71	−8.3	Conifer; 22.62 / 10.2
TC	Gain	142.86	10.2	−41.14	−3.0	48.16	63.9	81.81	77.2	54.09	45.7	Mixedwood; 81.81 / 77.2
BS	Gain	12.01	0.9	−124.80	−15.4	34.12	45.2	87.75	28.8	15.79	30.1	Mixedwood; 87.75 / 28.8

Percent changes are relative to each ecozone's 1986 baseline area for the class shown. Positive values indicate expansion; negative values indicate contraction. TUCO = Tundra Cordillera; HP = Hudson Plains; TP = Taiga Plains; BCO = Boreal Cordillera; TSE = Taiga Shield East; TC = Taiga Cordillera; BS = Boreal Shield. Dashes (–) indicate percentage is undefined due to a near-zero 1986 baseline or that sub-class change is small or not material to the main-contributor assessment in this condensed view.Which forest class (Conifer, Broadleaf, Mixedwood, or Wetland-treed) or shrub accounts for the majority of the net forest gain in that ecozone.

7 NDVI, Landcover and Climate, and Energy Flux Trend Relationship

In this section, we present supplementary information that supports the results discussed in Subsections 2.1 of the main paper. The subsection describe how observed vegetation type changes (Figures 4-5 and Table 6) are driven by climate trends (temperature and precipitation, Figure 8, Tables 9 10) and how, in turn, these vegetation shifts (influence seasonal (e.g Figures 9, 10 and Table 17 and annual energy flux patterns between 1986 and 2023 (Figure 11).

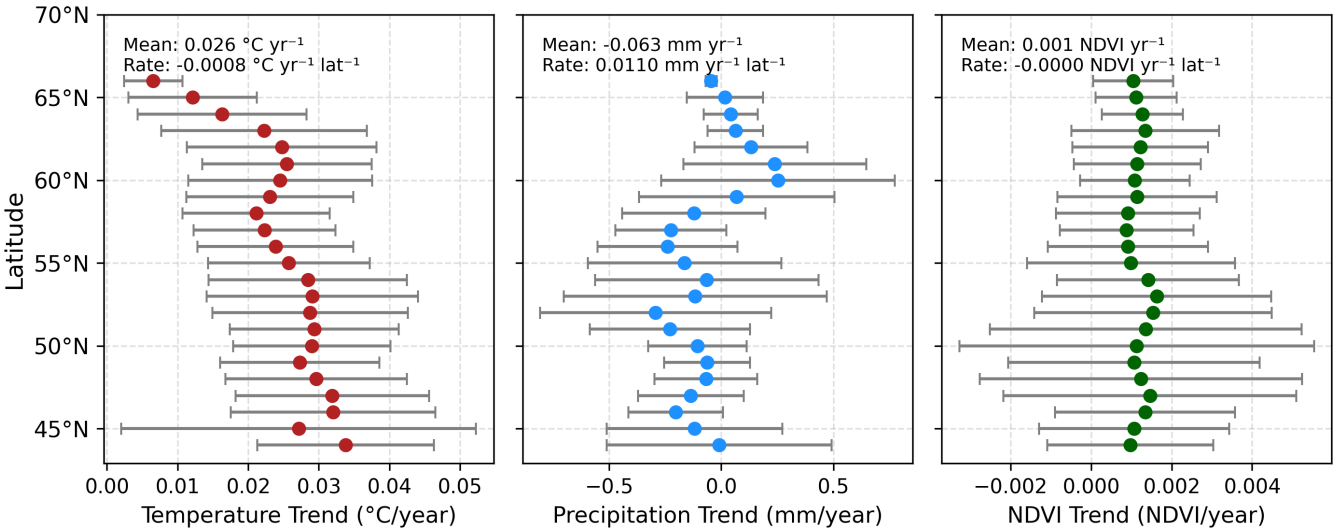


Fig. 8: Latitudinal trend of growing season temperature, precipitation, and NDVI (1986-2023). Individual points represent the mean statistically significant Theil-Sen trend for each latitude band. The horizontal bars indicate the plus or minus 1-standard deviation around the mean

7.1 Energy Feedbacks Observed Across the Ecozones

The supplementary presented here support the interpretation of results presented in Results subsection 2.3 of the main paper.

Table 7: Ecozone-level seasonal 2-m air temperature (T2m) metrics. For each season and ecozone, T_{1986}, long-term (1986-2023) mean T_{LT}, the 2023 deviation ΔT_{2023}, and the 2023 standardized anomaly σ_{anom} are reported.

Ecozone	Spring TA (°C)				Summer TA (°C)				Fall TA (°C)				Winter TA (°C)			
	T_{1986}	T_{LT}	ΔT_{2023}	σ_{anom}	T_{1986}	T_{LT}	ΔT_{2023}	σ_{anom}	T_{1986}	T_{LT}	ΔT_{2023}	σ_{anom}	T_{1986}	T_{LT}	ΔT_{2023}	σ_{anom}
SA	-15.05	-14.00	2.32	1.80	7.56	9.32	1.60	1.98	-9.09	-6.10	2.35	1.93	-25.31	-25.76	0.47	0.29
TP	-8.30	-6.49	0.79	0.52	8.23	9.67	0.82	0.93	-6.10	-5.08	1.42	1.20	-23.74	-21.67	0.64	0.37
BS	-0.04	-1.22	0.24	0.17	13.81	15.11	0.40	0.56	0.65	2.89	1.66	1.47	-16.91	-16.01	1.43	0.79
BC	-5.33	-3.71	-0.69	-0.49	9.97	10.83	0.82	1.34	-4.23	-3.40	1.31	1.10	-14.18	-16.94	0.12	0.06
TC	-11.62	-8.97	-0.75	-0.48	9.92	10.87	0.89	1.46	-8.76	-7.51	1.77	1.34	-19.51	-22.32	0.33	0.18
HP	-3.13	-4.71	0.08	0.05	12.66	14.01	0.35	0.44	-1.13	1.28	1.35	1.11	-21.92	-20.45	1.23	0.67
TSW	-9.62	-9.56	1.48	0.92	6.47	7.92	1.05	1.26	-7.56	-6.10	1.90	1.55	-24.58	-23.22	0.53	0.31
TUCO	-16.61	-12.91	-1.12	-0.64	5.04	7.45	1.23	1.57	-11.64	-9.01	1.92	1.42	-26.37	-27.45	0.29	0.19
TSE	-5.90	-6.00	1.53	0.96	11.53	12.45	0.61	0.77	-2.67	-1.85	1.58	1.22	-18.70	-17.90	0.98	0.54

Note. T_{LT} is the ecozone long-term seasonal mean over 1986–2023. $\Delta T_{2023} \equiv T_{2023} - T_{LT}$ (°C). $\sigma_{\text{anom}} \equiv (T_{2023} - T_{LT})/\sigma_{LT}$ (dimensionless), where σ_{LT} is the *sample* standard deviation of seasonal ecozone means over 1986–2023. T2m denotes near-surface (2-m) air temperature. T_{1986} is 1986 baseline mean. SA = Southern Arctic, TP = Taiga Plain, BS = Boreal Shield, BC = Boreal Cordillera, TC = Taiga Cordillera, HP = Hudson Plains, TSW = Taiga Shield West, TUCO = Tundra Cordillera, TSE = Taiga Shield East.

Table 8: Ecozone-level seasonal skin (land surface) temperature (Ts) metrics. For each season and ecozone, T_{1986}, long-term mean T_{LT}, the 2023 deviation ΔT_{2023}, and the 2023 standardized anomaly σ_{anom} are reported.

Ecozone	Spring Ts (°C)				Summer Ts (°C)				Fall Ts (°C)				Winter Ts (°C)			
	T_{1986}	T_{LT}	ΔT_{2023}	σ_{anom}	T_{1986}	T_{LT}	ΔT_{2023}	σ_{anom}	T_{1986}	T_{LT}	ΔT_{2023}	σ_{anom}	T_{1986}	T_{LT}	ΔT_{2023}	σ_{anom}
SA	-14.86	-13.12	3.57	2.27	8.13	10.29	3.27	2.51	-11.18	-7.36	3.94	2.19	-29.50	-29.52	-0.61	-0.32
TP	-8.56	-5.99	2.01	1.09	13.10	14.08	3.10	2.82	-6.06	-3.91	3.97	2.47	-23.62	-24.26	-0.95	-0.46
BS	0.08	-0.95	0.64	0.45	13.92	15.44	1.10	1.33	0.63	3.47	2.10	1.59	-16.87	-15.40	1.64	0.83
BC	-6.60	-5.24	0.29	0.20	9.68	11.08	2.34	2.28	-6.95	-6.52	2.86	1.91	-18.61	-21.52	1.11	0.59
TC	-12.86	-9.11	0.43	0.22	10.81	11.72	3.07	2.85	-12.44	-10.76	3.61	2.04	-24.08	-27.18	0.39	0.20
HP	-3.35	-4.20	0.40	0.20	12.62	14.67	1.73	1.68	-3.21	1.09	2.63	1.44	-22.94	-20.52	1.47	0.66
TSW	-9.37	-8.84	3.13	1.60	11.38	12.86	2.24	1.90	-6.63	-3.84	4.03	2.18	-26.98	-26.40	-0.19	-0.08
TCO	-15.94	-11.00	0.01	0.01	9.33	10.15	3.49	2.64	-13.59	-11.37	4.06	1.92	-27.44	-28.14	0.00	0.00
TSE	-7.05	-6.88	2.59	1.47	9.70	11.49	3.12	2.79	-4.30	0.19	2.32	1.59	-21.70	-20.95	1.33	0.53

Note. T_{LT} is the ecozone long-term seasonal mean over 1986–2023. $\Delta T_{2023} \equiv T_{2023} - T_{LT}$ (°C). $\sigma_{\text{anom}} \equiv (T_{2023} - T_{LT})/\sigma_{LT}$ (dimensionless), where σ_{LT} is the *sample* standard deviation of seasonal ecozone means over 1986–2023. Ts/LST denotes skin (land surface) temperature. T_{1986} is 1986 baseline mean. SA = Southern Arctic, TP = Taiga Plain, BS = Boreal Shield, BC = Boreal Cordillera, TC = Taiga Cordillera, HP = Hudson Plains, TSW = Taiga Shield West, TUCO = Tundra Cordillera, TSE = Taiga Shield East

Table 9: Growing season (June–September) correlation of NDVI trends with temperature and precipitation trends (significant Spearman correlations in **bold**).

Ecozone	**Area (10^3 km^2)**	**Corr (Temp)**	**Corr (Precip)**
Southern Arctic	4,273	**0.20**	-0.01
Taiga Plains	2,672	**-0.26**	**0.21**
Taiga Shield	5,146	**0.18**	**0.19**
Boreal Shield	6,191	0.01	**0.03**
Boreal Cordillera	2,287	0.00	-0.02
Taiga Cordillera	1,125	**0.06**	**0.08**
Hudson Plains	1,213	**-0.06**	**-0.07**
Tundra Cordillera	159	**0.06**	**0.10**

Spearman correlation coefficients; **bold** indicates $p < 0.05$. Corr (Temp) means correlation coefficeint between NDVI trend and temperature trend, Corr (Precip) means correlation coefficient between NDVI trend and Precipitation trend. Area is estimated geeodesically at 2.5-minute resolution and represents the proportion of each ecozone within which statistically significant correlations were observed.

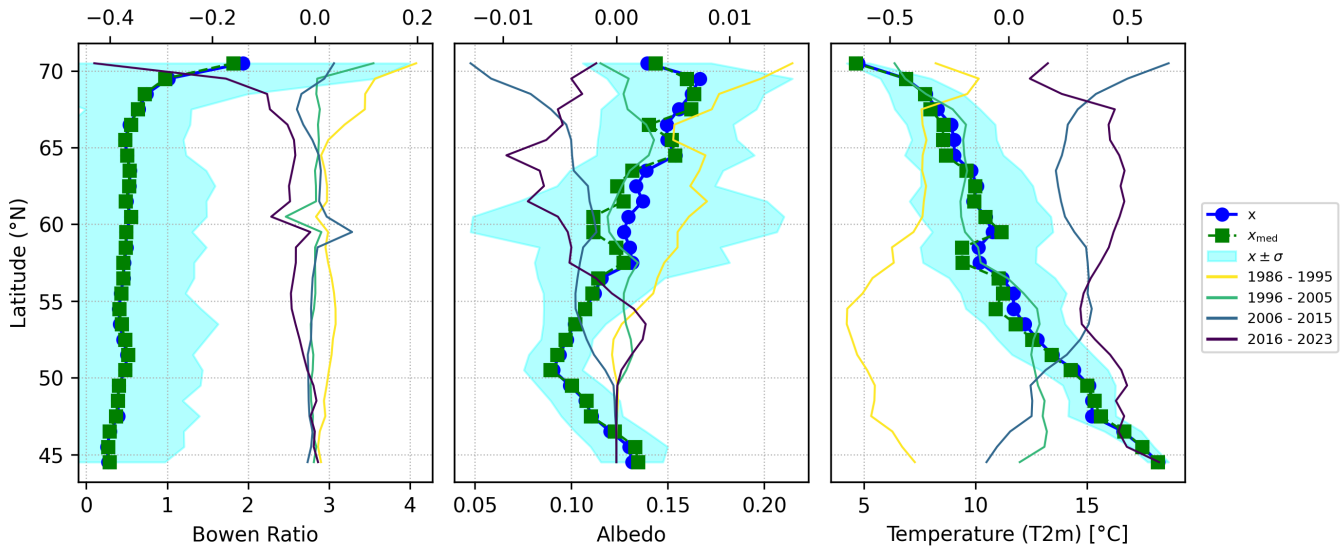


Fig. 9: Latitudinal means and decadal deviations of bowen ratio, albedo, and air temperature (T2m). The blue line with marker (X) represents individual mean values of each the three variable by latitude. The green squares (X_{med}) denote the median of each of three variable by latitude. Both values are plot on the down x-axis scale. The cyan shaded region ploton the down x-axis scale shows the mean value plus or minus standard deviation for each latitude band. Colored lines plotted on secons -x-axis at the top are the decadal deviation: 1986–1995 (purple), 1996–2005 (yellow), 2006–2015 (blue), and 2016–2023 (teal).

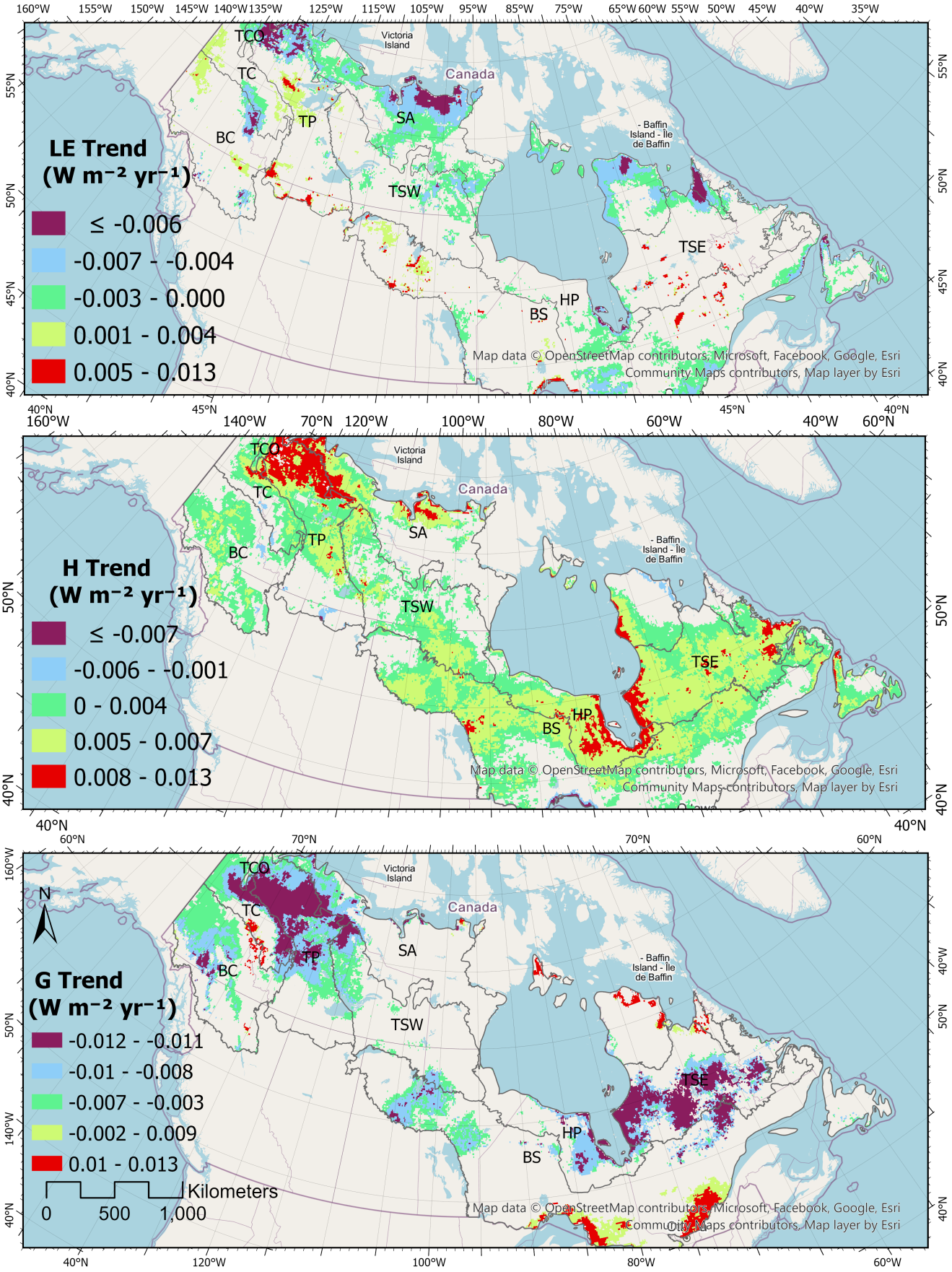


Fig. 10: Growing season (June–September) spatial distribution of statistically significant trends (1986-2023) in LE, H, and G across the study area. Plotted pixels denote locations with statistically significant linear trends. Black-bordered polygons indicate ecozone boundaries. SA = Southern Arctic, TP = Taiga Plain, BS = Boreal Shield, BC = Boreal Cordillera, TC = Taiga Cordillera, HP = Hudson Plains, TSW = Taiga Shield West, TCO = Tundra Cordillera, TSE = Taiga Shield East. Background basemap in all Panels: OpenStreetMap Style © OpenStreetMap contributors, Microsoft, Esri Community Maps contributors; rendered via Esri in ArcGIS Pro

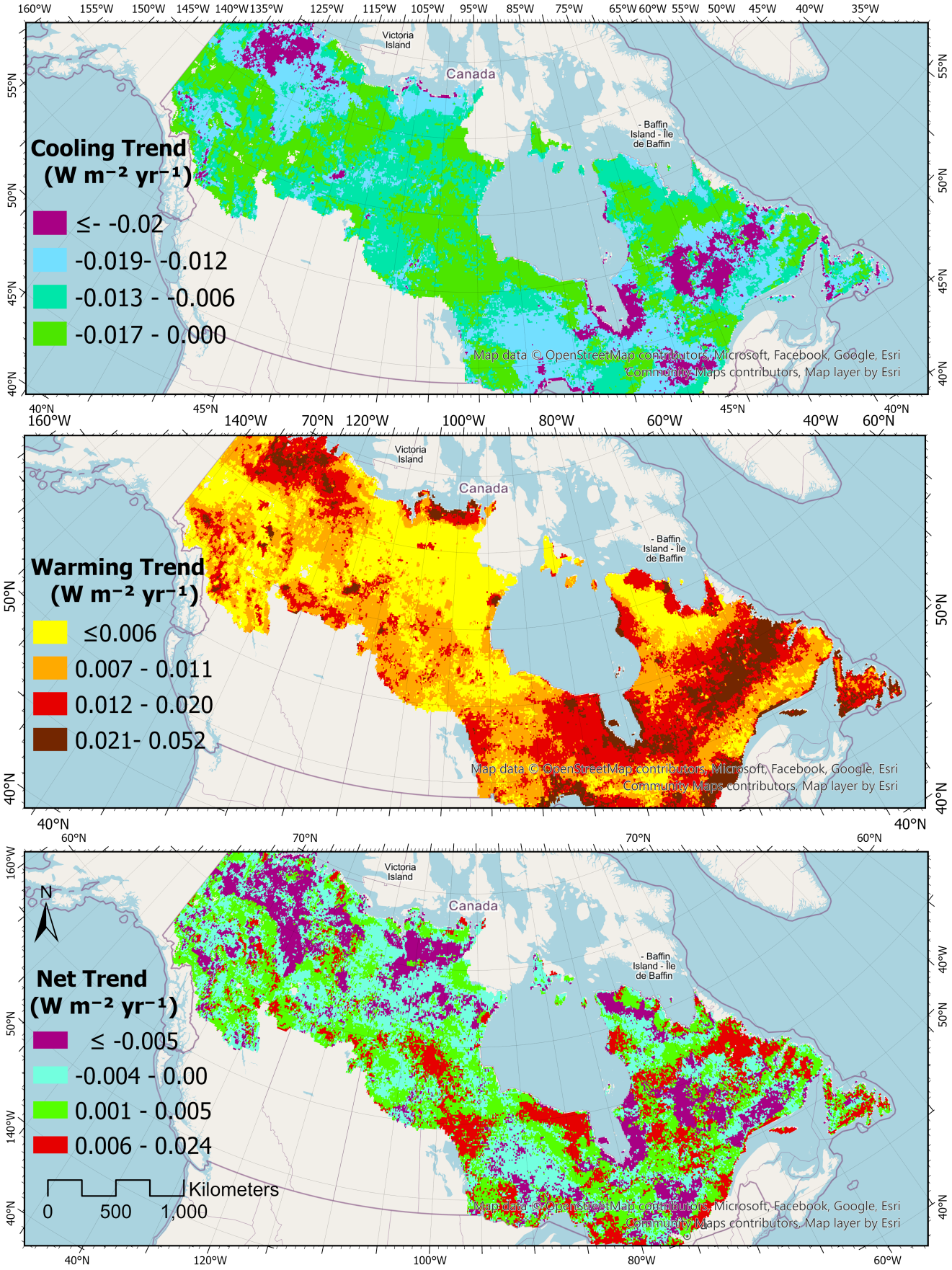


Fig. 11: Distribution of statistically annual integrated significant LE, H, G flux trends (1986-2023) into cooling, warming and net fluxes across the study area. Warming trend is the sum of all positive seasonal pixel-wise flux of LE, H, G while cooling trend is the sum of all positive seasonal pixel-wise flux of LE, H, G. Net trend is the sum of pixel-wise cooling and warming trend). Background basemap in all Panels: OpenStreetMap Style © OpenStreetMap contributors, Microsoft, Esri Community Maps contributors; rendered via Esri in ArcGIS Pro

Table 10: Growing Season (June–September) Spearman correlation coefficients (ρ) between NDVI trend and climate variables (temperature and precipitation) across 1° latitude bands from 44°N to 71°N. Bold values indicate statistically significant correlations ($p < 0.05$).

Lat (°N)	**Area ($\times 10^3$ km^2)**	**ρ (Temp)**	**ρ (Precip)**
44–45	37.26	-0.037	**-0.090**
45–46	127.57	0.014	**-0.091**
46–47	306.58	**-0.054**	-0.091
47–48	477.01	**-0.029**	**-0.060**
48–49	709.88	**-0.103**	**-0.090**
49–50	869.96	**-0.137**	**-0.091**
50–51	968.24	-0.007	**-0.017**
51–52	1034.75	**0.125**	**-0.016**
52–53	1029.32	**0.081**	**0.167**
53–54	1060.17	**0.091**	**0.154**
54–55	1063.57	**0.154**	**0.154**
55–56	1025.98	**0.170**	**0.153**
56–57	1082.29	**0.278**	**0.126**
57–58	1127.95	**0.212**	**0.137**
58–59	1019.58	**0.196**	**0.094**
59–60	1392.26	**0.095**	**0.092**
60–61	1422.73	**-0.093**	**0.064**
61–62	1385.08	**-0.097**	**-0.070**
62–63	1353.71	**-0.085**	**-0.091**
63–64	1199.84	-0.013	-0.090
64–65	1191.88	**0.078**	**-0.078**
65–66	1137.34	**0.128**	**-0.086**
66–67	654.00	**0.030**	**-0.058**
67–68	328.79	0.020	**-0.038**
68–69	15.30	**0.354**	**-0.265**

Note: Area is estimated assuming that a 2.5-minute pixel resolution is approximately 46.24 km^2 per pixel. Values represent the proportion of the latitude-band area where statistical significance was computed.

Table 11: Spearman correlations between NDVI trends (1986-2023) and seasonal temperature or precipitation trends across latitude bands (44°N–71°N).

	Temperature			**Precipitation**		
Latitude (°N)	Spring	Summer	Fall	Spring	Summer	Fall
44–45	-0.24** (9.7)	-0.15** (11.2)	-0.04 (11.2)	–	-0.09* (9.7)	0.12 (0.5)
45–46	-0.04 (29.9)	-0.02 (39.3)	-0.03 (39.3)	-0.21* (2.0)	-0.06* (18.7)	-0.04 (0.6)
46–47	-0.09** (55.9)	-0.06** (92.5)	-0.03* (92.6)	0.02 (44.5)	0.42** (3.6)	0.02 (6.9)
47–48	-0.23** (63.3)	0.03** (135.4)	-0.09** (137.2)	-0.21** (93.7)	0.38** (13.7)	-0.15** (62.8)
48–49	-0.05** (81.4)	-0.05** (187.3)	-0.17** (199.2)	-0.16** (158.1)	0.10** (31.4)	-0.00 (105.1)
49–50	-0.11** (116.2)	-0.13** (218.9)	-0.17** (229.9)	-0.14** (223.2)	0.11** (33.6)	-0.02 (100.9)
50–51	0.07** (118.4)	0.01 (246.1)	-0.06** (264.9)	-0.11** (222.6)	0.12** (12.7)	-0.09** (103.3)
51–52	0.26** (138.9)	0.21** (263.4)	-0.14** (275.8)	-0.27** (221.2)	0.04* (36.5)	-0.09** (146.7)
52–53	0.24** (149.5)	0.20** (227.2)	-0.17** (268.9)	-0.13** (139.6)	0.08** (67.1)	0.01 (195.0)
53–54	0.29** (141.3)	0.21** (197.0)	-0.16** (264.7)	-0.02 (103.3)	0.11** (79.5)	-0.02* (199.2)
54–55	0.36** (182.1)	0.18** (193.0)	-0.08** (270.6)	0.12** (95.9)	0.19** (111.9)	0.00 (197.3)
55–56	0.34** (235.7)	0.27** (164.0)	0.12** (257.2)	0.03* (76.1)	0.27** (80.8)	-0.17** (209.2)
56–57	0.28** (234.7)	0.27** (147.3)	0.11** (233.8)	-0.16** (64.4)	-0.06** (72.4)	-0.12** (176.4)
57–58	0.26** (213.9)	0.33** (188.4)	0.12** (223.7)	-0.33** (62.6)	-0.14** (115.6)	-0.27** (193.0)
58–59	0.28** (179.2)	0.30** (214.1)	0.15** (230.0)	-0.39** (43.9)	-0.08** (88.6)	-0.27** (162.2)
59–60	0.19** (136.0)	0.12** (266.2)	0.21** (276.8)	-0.25** (46.5)	0.12** (43.9)	-0.20** (95.8)
60–61	0.16** (77.7)	-0.01 (292.2)	0.09** (305.7)	-0.09** (49.4)	-0.10** (66.2)	-0.37** (101.1)
61–62	0.01 (29.4)	-0.12** (276.6)	-0.01 (297.3)	0.04* (44.7)	-0.10** (71.5)	-0.13** (79.6)
62–63	-0.05* (18.5)	-0.19** (235.4)	-0.03** (265.4)	-0.13** (47.0)	0.06** (85.4)	-0.01 (37.7)
63–64	-0.28** (11.9)	-0.04** (231.3)	-0.08** (259.3)	0.12** (108.1)	0.11** (124.2)	0.09** (35.0)
64–65	-0.02 (2.9)	0.01 (231.7)	-0.02* (237.2)	0.08** (149.6)	0.03** (129.7)	-0.11** (49.7)
65–66	0.13* (3.1)	0.01 (217.3)	0.04** (217.1)	0.05** (156.6)	0.01 (126.3)	-0.33** (35.5)
66–67	0.07* (13.3)	0.08** (197.7)	0.06** (209.7)	0.10** (148.1)	0.04** (115.7)	-0.02 (14.1)
67–68	0.11** (34.8)	0.08** (153.2)	-0.11** (189.7)	0.21** (123.4)	-0.06** (102.1)	-0.04* (35.3)
68–69	-0.04* (25.7)	0.13** (77.1)	-0.01 (118.8)	0.15** (61.8)	0.06** (81.6)	-0.07** (26.4)
69–70	0.24** (6.0)	-0.13** (22.3)	0.11** (47.9)	-0.09** (19.4)	-0.02 (14.8)	-0.03 (11.8)
70–71	–	-0.23 (0.2)	-0.12 (1.8)	–	–	–

Values are Spearman correlation coefficients (r) between NDVI trends (1986–2023) and seasonal temperature or precipitation trends. Values in parentheses indicate the land surface area (10^3 km^2) of valid pixels used in each correlation. Statistical significance is denoted by ** ($p < 0.01$) and * ($p < 0.05$). Pixel areas were estimated using a geodesic approach, converting raster resolution (0.041667°) to true surface area on a spherical Earth (radius = 6371 km), accounting for latitudinal variation in pixel size.

Table 12: Area coverage (in 10^3 km^2) of statistically significant ($p < 0.05$) seasonal trends in temperature and precipitation by latitude band. These areas within the corresponding latitudinal per seasons from which the corresponding statistically significant linear trend reported Figure 5 a and b (Main paper) and their uncertainty ranges were estimated.

	Temperature				Precipitation			
Latitude Band	Fall	Spring	Summer	Winter	Fall	Spring	Summer	Winter
44–45°N	12.14	10.36	12.14	12.14	0.49	nan	10.44	12.14
45–46°N	41.19	31.50	41.19	41.19	0.58	2.29	20.00	41.19
46–47°N	97.41	59.11	97.26	97.41	7.88	47.61	4.32	89.44
47–48°N	146.93	69.46	144.65	145.67	68.46	102.01	14.73	72.53
48–49°N	215.99	87.40	202.79	168.79	114.45	172.15	34.42	156.98
49–50°N	244.52	124.06	232.37	134.54	109.75	239.32	35.94	217.25
50–51°N	280.90	123.26	261.09	145.28	110.31	236.60	13.54	267.89
51–52°N	292.55	145.56	279.06	168.43	154.83	234.34	38.65	230.00
52–53°N	287.52	157.18	243.62	174.33	207.88	148.92	73.49	140.41
53–54°N	277.16	146.45	207.08	157.38	208.61	106.44	84.74	122.16
54–55°N	285.27	191.81	205.44	166.87	207.08	98.80	116.10	162.33
55–56°N	268.25	245.72	172.54	125.79	218.36	78.91	83.45	149.80
56–57°N	243.84	244.87	155.68	103.06	184.69	68.04	75.29	112.86
57–58°N	234.40	223.31	199.27	94.71	202.46	65.61	121.66	128.33
58–59°N	242.51	187.58	226.96	83.53	170.85	46.49	94.77	121.97
59–60°N	293.93	142.19	283.15	65.91	104.19	52.38	47.42	175.45
60–61°N	317.07	79.66	303.15	58.76	106.70	53.49	69.18	186.07
61–62°N	307.13	29.98	286.10	43.79	84.16	47.21	73.53	154.86
62–63°N	280.46	19.65	247.85	29.17	41.17	48.99	90.53	154.72
63–64°N	273.18	12.72	243.04	20.90	36.23	113.32	130.63	121.91
64–65°N	227.13	3.18	241.35	30.12	52.50	155.29	135.14	128.75
65–66°N	219.76	13.67	227.45	35.07	36.84	164.42	129.79	154.06
66–67°N	198.81	37.12	207.55	39.49	14.48	156.23	118.54	87.95
67–68°N	125.22	28.90	161.56	50.79	36.28	129.44	105.16	77.60
68–69°N	51.42	6.65	82.32	35.82	26.92	65.91	85.75	48.68
69–70°N	1.92	nan	0.20	nan	12.76	21.12	15.88	15.54
70–71°N	–	–	–	–	0.42	nan	nan	0.04

Table 13: Seasonal temperature (T2m) trends, affected area fractions, and total impact across CBT ecozones (1986–2023).

		Temperature (°C yr^{-1}) (% Area in brackets)				
Eco	**Area (10^3 km^2)**	**Spring**	**Summer**	**Fall**	**Winter**	**Impact**
SA	949	0.02 (24)	0.04 (88)	0.05 (84)	0.06 (43)	10.13
TP	554	-0.02 (1)	0.03 (20)	0.04 (19)	-0.02 (4)	1.27
BS	1 893	-0.02 (7)	0.02 (22)	0.05 (21)	0.06 (48)	4.22
BC	558	-0.02 (1)	0.02 (15)	0.04 (14)	0.01 (1)	0.87
TC	231	-0.02 (1)	0.02 (15)	0.05 (22)	0.03 (7)	1.57
HP	350	-0.04 (5)	0.01 (8)	0.04 (8)	0.03 (15)	0.69
TSW	619	-0.03 (3)	0.03 (10)	0.05 (10)	0.02 (1)	0.67
TUCO	29	-0.02 (3)	0.01 (12)	0.08 (12)	0.03 (46)	2.43
TSE	702	0.03 (14)	0.04 (26)	0.05 (24)	0.07 (76)	8.13

Note: *Impact* represents the spatially weighted warming intensity for each ecozone, computed as the sum of seasonal temperature trends multiplied by the geodesically derived fraction of significantly warming pixels within that ecozone (Trend × % area). The percentage value in brackets beside each trend indicates the proportion of the ecozone area exhibiting statistically significant warming (Mann–Kendall, $p < 0.05$). Eco: SA = Southern Arctic, TP = Taiga Plain, BS = Boreal Shield, BC = Boreal Cordillera, TC = Taiga Cordillera, HP = Hudson Plains, TSW = Taiga Shield West, TUCO = Tundra Cordillera, TSE = Taiga Shield East.

Table 14: Spring and Summer Baseline 1986 seasonal fluxes. Units are in W m^{-2}.

Eco	**Spring**			**Summer**		
	LE	**H**	**G**	**LE**	**H**	**G**
SA	-0.29 ± 0.09	-0.13 ± 0.19	0.84 ± 0.44	-1.55 ± 0.26	-1.06 ± 0.44	5.81 ± 0.75
TP	-0.44 ± 0.22	-0.81 ± 0.49	3.09 ± 1.16	-1.72 ± 0.60	-1.39 ± 0.62	7.83 ± 0.81
BS	-0.91 ± 0.25	-1.16 ± 0.42	4.76 ± 1.04	-2.67 ± 0.47	-1.23 ± 0.39	8.14 ± 0.79
BC	-0.26 ± 0.15	-0.86 ± 0.47	2.79 ± 1.10	-1.86 ± 0.37	-1.29 ± 0.32	7.42 ± 0.89
TC	-0.14 ± 0.10	-0.75 ± 0.52	2.40 ± 1.20	-1.64 ± 0.29	-1.08 ± 0.22	6.97 ± 0.74
HP	-0.77 ± 0.17	-1.43 ± 0.53	2.83 ± 1.20	-2.36 ± 0.20	-1.52 ± 0.31	7.51 ± 0.38
TSW	-0.45 ± 0.17	-0.42 ± 0.42	2.42 ± 1.21	-2.15 ± 0.26	-1.05 ± 0.37	7.25 ± 0.73
TCO	-0.32 ± 0.03	-0.94 ± 0.41	2.70 ± 0.78	-1.81 ± 0.22	-1.28 ± 0.18	6.89 ± 0.37
TSE	-0.52 ± 0.14	-0.55 ± 0.57	2.35 ± 1.17	-1.90 ± 0.26	-0.91 ± 0.38	5.99 ± 0.55

ERA5-Land sign convention: positive downward (toward the surface), negative upward. Values are reported as mean ± s.d. and are computed only over pixels that exhibit a statistically significant trend (1986–2023) in the corresponding flux; this significance mask was applied to the 1986 seasonal LE, H, and G fields before spatial averaging. G is computed per month as $R_n - \mathrm{LE} - \mathrm{H}$ (after unit conversion to W m^{-2}) and then seasonally averaged. Eco: SA = Southern Arctic, TP = Taiga Plain, BS = Boreal Shield, BC = Boreal Cordillera, TC = Taiga Cordillera, HP = Hudson Plains, TSW = Taiga Shield West, TUCO = Tundra Cordillera, TSE = Taiga Shield East.

Table 15: Fall and Winter Baseline 1986 seasonal fluxes. Units are in W m^{-2}.

Eco	**Fall**			**Winter**		
	LE	**H**	**G**	**LE**	**H**	**G**
SA	-0.30 ± 0.17	0.03 ± 0.11	0.09 ± 0.33	0.03 ± 0.08	0.51 ± 0.12	-1.30 ± 0.41
TP	-0.37 ± 0.24	-0.22 ± 0.14	0.76 ± 0.57	-0.04 ± 0.12	0.34 ± 0.12	-0.93 ± 0.33
BS	-0.98 ± 0.22	-0.49 ± 0.24	2.13 ± 0.36	-0.16 ± 0.15	0.07 ± 0.11	-0.22 ± 0.24
BC	-0.34 ± 0.22	-0.21 ± 0.21	1.00 ± 0.33	0.02 ± 0.14	0.21 ± 0.08	-0.72 ± 0.26
TC	-0.21 ± 0.12	0.03 ± 0.08	0.29 ± 0.26	0.02 ± 0.10	0.15 ± 0.06	-0.52 ± 0.22
HP	-0.62 ± 0.17	-0.27 ± 0.13	0.95 ± 0.30	-0.06 ± 0.08	0.06 ± 0.10	-0.66 ± 0.26
TSW	-0.55 ± 0.17	-0.26 ± 0.12	0.96 ± 0.27	-0.01 ± 0.08	0.34 ± 0.11	-0.92 ± 0.30
TCO	-0.24 ± 0.10	0.14 ± 0.07	0.03 ± 0.16	0.01 ± 0.07	0.10 ± 0.06	-0.41 ± 0.25
TSE	-0.77 ± 0.18	-0.24 ± 0.12	1.24 ± 0.33	-0.04 ± 0.09	0.11 ± 0.06	-0.60 ± 0.24

ERA5-Land sign convention: positive downward (toward the surface), negative upward. Values are reported as mean ± s.d. and are computed only over pixels that exhibit a statistically significant trend (1986–2023) in the corresponding flux; this significance mask was applied to the 1986 seasonal LE, H, and G fields before spatial averaging. G is computed per month as $R_n - \mathrm{LE} - \mathrm{H}$ (after unit conversion to W m^{-2}) and then seasonally averaged. Eco: SA = Southern Arctic, TP = Taiga Plain, BS = Boreal Shield, BC = Boreal Cordillera, TC = Taiga Cordillera, HP = Hudson Plains, TSW = Taiga Shield West, TUCO = Tundra Cordillera, TSE = Taiga Shield East.

Table 16: The 1986 mean annual Energy fluxes of CBT ecozones, with linear NET trend as at 2023.

	Fluxes (W m^{-2})				Trend	Δ 37 yr	% Change
Eco	**LE**	**H**	**G**	**NET$_{86}$**			
SA	-0.51 ± 0.05	-0.15 ± 0.05	1.40 ± 0.24	0.74 ± 0.14	−0.006	−0.222	−30.00%
TP	-0.79 ± 0.07	-0.51 ± 0.07	2.66 ± 0.30	1.36 ± 0.18	−0.009	−0.333	−24.49%
BS	-1.16 ± 0.08	-0.69 ± 0.05	3.76 ± 0.29	1.92 ± 0.17	0.000	0.000	0.00%
BC	-0.67 ± 0.07	-0.52 ± 0.05	2.51 ± 0.27	1.32 ± 0.15	−0.003	−0.111	−8.41%
TC	-0.62 ± 0.07	-0.38 ± 0.05	2.10 ± 0.26	1.09 ± 0.14	−0.006	−0.222	−20.37%
HP	-0.94 ± 0.08	-0.65 ± 0.07	3.23 ± 0.30	1.64 ± 0.16	0.006	0.222	13.54%
TSW	-0.77 ± 0.07	-0.33 ± 0.05	2.29 ± 0.27	1.18 ± 0.16	−0.003	−0.111	−9.41%
TCO	-0.54 ± 0.06	-0.43 ± 0.07	2.01 ± 0.26	1.03 ± 0.15	−0.006	−0.222	−21.55%
TSE	-0.79 ± 0.06	-0.28 ± 0.05	2.24 ± 0.24	1.17 ± 0.14	0.003	0.111	9.49%

ERA5-Land sign convention: positive downward (toward surface), negative upward (away from surface). LE, H, G, and NET$_{86}$ values are mean ± s.d. in W m^{-2}. G is computed per month as $R_n - \mathrm{LE} - \mathrm{H}$ after conversion to W m^{-2}, then annually averaged; $\mathrm{NET}_{86} = \mathrm{LE} + \mathrm{H} + G$ for the year 1986. **Trend** is the ecozone NET slope (W m^{-2} yr^{-1}) referenced in the main paper Table 3, column 8; Δ 37 yr = Trend ×37 (1986→2023); % Change = 100 × Δ/NET$_{86}$. Eco: SA = Southern Arctic, TP = Taiga Plain, BS = Boreal Shield, BC = Boreal Cordillera, TC = Taiga Cordillera, HP = Hudson Plains, TSW = Taiga Shield West, TUCO = Tundra Cordillera, TSE = Taiga Shield East.

8 Albedo Estimation and Trends

We estimated surface shortwave albedo from the MODIS BRDF/Albedo product suite (Collection 6.1) in GEE. Daily MCD43A3 (v061) granules were the primary albedo source, and MCD43A2 (v061) provided snow flags for quality control. Processing covered meteorological years (MetYears) from 1 December 2000 to the last complete MetYear available at the time of analysis. A MetYear Y spans 1 December Y to 30 November $Y{+}1$, partitioned into DJF (Dec–Feb), MAM (Mar–May), JJA (Jun–Aug), and SON (Sep–Nov).

Blue-sky albedo

MODIS reports black-sky (BSA; direct beam) and white-sky (WSA; diffuse) shortwave albedos (α). To approximate real-sky conditions, we formed blue-sky albedo as

$$\alpha_{\text{blue}} \;=\; f\,\alpha_{\text{WSA}} \;+\; (1-f)\,\alpha_{\text{BSA}},$$

where f is the diffuse fraction of incoming shortwave radiation ($0{\le}f{\le}1$). Unless otherwise specified, we set $f = 0.5$, noting that a spatiotemporal f field from reanalysis could further tailor this mixture. All albedo bands were converted to unitless reflectance using the published scale factor ($\times 0.001$).

Quality control and vegetation-only versus vegetation–snow albedo estimation

We retained pixels with Mandatory Shortwave QA ≤ 0 (best quality) from MCD43A3; where coverage was sparse, a sensitivity analysis relaxed this to QA ≤ 1 (good+best). To obtain snow-free albedo, we removed pixels flagged as snow in the temporally matched MCD43A2 granule (`Snow_BRDF_Albedo` = 1). When no suitable A2 granule was available for a given day, snow masking for that day was skipped to avoid false exclusions. For vegetation-snow we deactivated snow masking making sure snow were included. All outputs (snow-free versus vegetation-snow)were intersected with a native analysis footprint derived from an ancillary mask (`Net_trend_clip`), ensuring spatial consistency across products.

Uncertainty-weighted temporal means

For each scenario (snow-free versus vegetation-snow) and temporal window (annual and seasonal), we composited daily albedo to a mean image using inverse-variance weights when the corresponding per-pixel shortwave albedo uncertainty band was available:

$$\bar{\alpha} \;=\; \frac{\sum_i \alpha_i\, w_i}{\sum_i w_i}, \qquad w_i \;=\; \sigma_i^{-2},$$

where σ_i is the product-reported uncertainty for day i. If uncertainty was missing, we defaulted to an unweighted mean.

Spatial summarization

For each scenario (snow-free versus vegetation-snow) and temporal window, the mean albedo image was reduced over Ecozone polygons at 500 m nominal scale. We then obtained the Ecozone mean, standard deviation, minimum, maximum, median, percentiles (p10, p25, p75, p90), valid-pixel count, the coefficient of variation (CV = std/mean; null-safe), and interquartile range (IQR = p75−p25).

Baseline anomalies

We quantified deviations from an early reference period (MetYear 2000-12-01 to 2001-11-30) by computing, for each polygon and period, the absolute anomaly $\Delta\alpha = \bar{\alpha} - \bar{\alpha}_0$, the percent anomaly $(\Delta\alpha/\bar{\alpha}_0)\times 100$ (guarded where $\bar{\alpha}_0 > 0$), and a z-score $(\bar{\alpha} - \bar{\alpha}_0)/\text{std}$ (guarded where std> 0). Baseline is matched within the same product label and period.

Albedo Trends

For each scenario (snow-free versus vegetation-snow) and temporal period (Annual, DJF, MAM, JJA, SON), we assembled a time series of period-mean albedo images with an auxiliary homogeneous "year" band, then estimated pixel-wise trends using (i) Theil–Sen slope (robust median-of-slopes) and (ii) ordinary least squares (OLS) slope with coefficient of determination R^2. We also expressed relative change as percent per decade by normalizing the OLS

slope by the first MetYear's period mean and multiplying by 10 (masked where the baseline ≤ 0). Ecozone-level summaries included the mean and median Theil–Sen slope, mean OLS slope, mean R^2, mean percent-per-decade, and the fractions of pixels with positive and negative Theil–Sen slopes.

Table 17: Ecozone summer energy, temperature, snow-free albedo and precipitation trends.

Eco	TR_{n86}	ΔR_n	TR_{n23}	Offset	Drivers	Temp		Albedo		Disturb	Precip
						T_a	T_s	JJA	Ann.		
BS	4.24	0.0040	4.39	No	$G\downarrow$, $H\downarrow$, LE$\uparrow$ (inward heating dominates)	0.03	0.02	0.56	0.62	162.0	0.55
HP	3.63	-0.0080	3.33	Yes	$G\uparrow\uparrow$, LE$\uparrow$, $H\downarrow$ (outward losses dominate)	0.02	0.02	0.19	0.54	11.4	0.55
TSE	3.18	-0.0060	2.96	Yes	$G\uparrow\uparrow$, LE$\uparrow$, $H\downarrow$ (outward losses dominate)	0.05	0.04	-0.40	-0.26	33.9	1.11
SA	3.20	-0.0002	3.19	Neutral	$H\downarrow$, $G\uparrow$, LE$\uparrow$ (inward heating offsets cooling)	0.05	0.05	0.51	0.38	0.08	0.38
TP	4.72	-0.0080	4.42	Yes	$G\uparrow$, LE$\uparrow$, $H\downarrow$ (outward cooling exceeds modest inward heating)	0.03	0.03	0.29	0.15	123.1	0.34
BC	4.27	-0.0060	4.05	Yes	$G\uparrow$, LE$\uparrow$, $H\downarrow$ (same as TP)	0.03	0.03	0.10	-0.02	25.5	0.65
TSW	4.05	-0.0090	3.72	Yes	$G\uparrow$, LE$\uparrow$, $H\downarrow$ (same as TP)	0.04	0.04	0.78	0.64	54.1	0.31
TC	4.25	-0.0070	3.99	Yes	$G\uparrow\uparrow$, LE$\uparrow$, $H\downarrow$ (large outward losses cancel heating)	0.02	0.02	0.54	0.50	0.11	0.48
TUCO	3.80	-0.0090	3.47	Yes	$G\uparrow\uparrow$, LE$\uparrow$, $H\downarrow$ (large outward losses cancel heating)	0.02	0.01	0.81	0.73	0.00	0.97

Abbreviations and units. TR_{n86}: net summer energy flux in 1986 ($\mathrm{W\,m^{-2}}$). TR_{n23}: net summer energy flux in 2023 ($\mathrm{W\,m^{-2}}$). ΔTR_n: net summer energy-flux trend ($\mathrm{W\,m^{-2}\,yr^{-1}}$). JJA = June–August. *Offset*: net summer radiative offset (Yes if trend < 0). *Drivers*: $\downarrow$ indicates inward surface-energy gain (warming tendency), whereas $\uparrow$ indicates outward surface-energy loss (cooling tendency). Double arrows indicate comparatively larger magnitudes. T_a and T_s are air- and surface-temperature trends ($^\circ\mathrm{C\,yr^{-1}}$). Albedo (JJA and Annual) is reported as $\%\,\mathrm{decade^{-1}}$ (2000–2023). Disturbance represents FIRE + HARVEST totals scaled by $\times 10^3$ (1986–2020). Precipitation is the Theil–Sen slope ($\mathrm{mm\,yr^{-2}}$). SA = Southern Arctic; TP = Taiga Plain; BS = Boreal Shield; BC = Boreal Cordillera; TC = Taiga Cordillera; HP = Hudson Plains; TSW = Taiga Shield West; TUCO = Tundra Cordillera; TSE = Taiga Shield East.

Table 18: Ecozone level vegetation-snow albedo percent decade change across CBT ecozones.

Eco	Annual	DJF	MAM	JJA	SON
BS	-0.43 ± 26.97 [-0.45, -0.42]	3.85 ± 18.29 [3.83, 3.86]	3.33 ± 43.98 [3.31, 3.36]	0.30 ± 12.51 [0.29, 0.31]	-0.27 ± 7.55 [-0.27, -0.26]
HP	0.46 ± 9.16 [0.45, 0.47]	2.85 ± 10.96 [2.82, 2.89]	2.26 ± 35.00 [2.21, 2.30]	0.05 ± 2.90 [0.04, 0.05]	-0.88 ± 8.70 [-0.89, -0.87]
TSE	1.63 ± 27.83 [1.61, 1.66]	0.12 ± 12.31 [0.10, 0.15]	-1.35 ± 37.23 [-1.38, -1.31]	-0.47 ± 11.06 [-0.48, -0.46]	0.06 ± 10.45 [0.04, 0.08]
SA	14.29 ± 26.53 [14.27, 14.30]	-1.24 ± 3.65 [-1.32, -1.16]	12.19 ± 38.58 [12.15, 12.23]	0.22 ± 16.63 [0.21, 0.24]	12.82 ± 31.74 [12.80, 12.85]
TP	1.94 ± 25.84 [1.91, 1.96]	5.61 ± 14.18 [5.59, 5.63]	-3.96 ± 14.48 [-3.97, -3.94]	0.14 ± 21.70 [0.12, 0.16]	-2.34 ± 11.67 [-2.35, -2.33]
BC	-5.49 ± 17.23 [-5.50, -5.47]	1.82 ± 16.22 [1.79, 1.84]	-2.63 ± 11.82 [-2.64, -2.61]	-0.02 ± 6.40 [-0.02, -0.01]	0.96 ± 9.97 [0.95, 0.98]
TSW	7.33 ± 24.87 [7.31, 7.35]	10.35 ± 14.78 [10.31, 10.38]	8.05 ± 44.07 [8.01, 8.09]	-0.10 ± 15.12 [-0.11, -0.08]	-0.51 ± 14.96 [-0.52, -0.50]
TC	0.56 ± 11.48 [0.55, 0.58]	2.56 ± 13.16 [2.52, 2.60]	0.58 ± 8.07 [0.57, 0.59]	0.66 ± 4.87 [0.66, 0.67]	-3.17 ± 16.22 [-3.19, -3.14]
TUCO	5.95 ± 9.66 [5.92, 5.99]	-0.05 ± 9.01 [-0.15, 0.05]	-0.01 ± 5.15 [-0.03, 0.01]	0.92 ± 2.16 [0.92, 0.93]	2.18 ± 17.13 [2.12, 2.25]

Note: Values are ecozone-level mean percent decade changes in BSA shortwave albedo, reported as mean ± standard deviation across pixels within each ecozone, with pixel-based 95% confidence intervals in brackets. Ecozone order is BS = Boreal Shield, HP = Hudson Plains, TSE = Taiga Shield East, SA = Southern Arctic, TP = Taiga Plain, BC = Boreal Cordillera, TSW = Taiga Shield West, TC = Taiga Cordillera, and TUCO = Tundra Cordillera.

Table 19: Ecozone-level association between positive NDVI trends and net energy flux trends

Ecozone	N	τ	p-value
BC	97,708	-0.00	0.1699
BS	60,260	-0.11	0.00
HP	96,607	-0.00	0.3155
SA	96,090	-0.05	1.04e-130
TC	99,455	-0.04	4.95e-88
TUCO	97,616	-0.03	1.60e-41
TP	95,328	-0.26	< 1e-300
TSE	97,816	0.17	< 1e-300
TSW*	14,717	-0.12	3.09e-100

Each ecozone Kendall's τ rank is the monotonic correlation between NDVI trend and net energy flux trend derived using unique, non-overlapping 30 m raster cells after four independent sampling–correlation round analyses, for which NDVI trends are greater than zero or 0.0015. By default, results based on samples drawn where NDVI trends are greater than 0.0000 were retained unless higher NDVI-trend thresholds showed a stronger and statistically significant negative association supported by sufficient sample size. *N* denotes the number of valid sampled cells within the ecozone after masking and filtering used for analysis. The asterisk (*) indicates the ecozone where a higher NDVI threshold was used. SA = Southern Arctic, TP = Taiga Plain, BS = Boreal Shield, BC = Boreal Cordillera, TC = Taiga Cordillera, HP = Hudson Plains, TSW = Taiga Shield West, TUCO = Tundra Cordillera, TSE = Taiga Shield East.

Table 20: Comparison of net energy flux trend (W m^{-2} yr^{-1}) between stable and greening vegetation zones.

Round	N (Stable)	N (Greening)	Welch t	p-value (t)	Mann–Whitney U	p-value (U)
1	840	191	−2.276	0.0236	71 697	0.0218
2	3 378	656	−3.050	0.00235	1 013 773	0.000558
3	840	191	−2.276	0.0236	71 697	0.0218
4	3 378	656	−3.050	0.00235	1 013 773	0.000558
5	4 218	847	−3.871	0.000118	1 473 002	0.000053

Note: Each sampling round represents an independent random draw of non-overlapping 30 m cells of net energy flux trend from the full study area, stratified into stable (no vegetation transition) and greening (vegetation transition) zones. Net flux energy trend values were compared between the two vegetation states using Welch's t-test and the non-parametric Mann–Whitney U test. Sample size varies across rounds due to the randomized, non-replacement spatial sampling design.

9 Data availability

The datasets generated and analysed during this study are available in Zenodo under DOI: 10.5281/zenodo.20656242.

The data used in this study are publicly available from the following sources. Landsat 5, 7, 8, and 9 Collection 2 Level-2 surface reflectance data were retrieved from Google Earth Engine (GEE) via `LANDSAT/LT05/C02/T1_L2`, `LANDSAT/LE07/C02/T1_L2`, `LANDSAT/LC08/C02/T1_L2`, and `LANDSAT/LC09/C02/T1_L2`. Ecozone polygons were obtained from Agriculture and Agri-Food Canada (https://sis.agr.gc.ca/cansis/nsdb/ecostrat/gis_data.html). National Fire Database (NFDB) data were obtained from the Canadian Wildland Fire Information System Data Mart (https://cwfis.cfs.nrcan.gc.ca/datamart). ERA5-Land monthly data were accessed through GEE (`ECMWF/ERA5_LAND/MONTHLY`). Downscaled CRU TS v4.09 monthly climate fields were obtained from WorldClim (https://www.worldclim.org/data/monthlywth.html). Global Land Cover Fine Classification (GLC-FCS30D) products were accessed through GEE via `projects/sat-io/open-datasets/GLC-FCS30D/annual` and `projects/sat-io/open-datasets/GLC-FCS30D/five-years-map`. The Canada annual land-cover (VLCE v2) dataset was accessed via `projects/sat-io/open-datasets/CA_FOREST_LC_VLCE2`. Albedo data were obtained from MODIS MCD43A3 v061 (`MODIS/061/MCD43A3`) and associated quality information from MCD43A2 v061 (`MODIS/061/MCD43A2`).

10 Code availability

The code generated and used during this study is available in the Borealis Dataverse repository under DOI: 10.5683/SP4/GHGQXM and through GitHub at https://github.com/danielamaogu/Boreal-Tundra-Vegetation-Increase-Effects-on-Surface-Cooling-and-Warming-Tendencies.

11 Acknowledgements

We will like to thank Dr. Tim Elrick the Director of Geographic Information Centre, McGill University, for providing access to advanced computing systems that supports the volume computation presented this study.

12 Funding Statement

This research was primarily funded by the Natural Sciences and Engineering Research Council of Canada (NSERC) (ALLRP 576419-22), PRIMA Québec, BGC Engineering Inc., Awn Nanotech, and Object Research Systems (P.M.) and the NSERC Alliance Mission grant (ALLRP 577126-2022) (Y.L., R.B., P.M., and J.M.-C.). We also acknowledge the Fond de Research Doctoral Scholarship (doi.org/10.69777/368830) that support DCA studies and part of this research.

13 Author Contribution Statement

D.C.A. conducted the research, literature review, wrote the article, plotted results, and created illustrations. P.M. was involved in ideation, conceptualization, setting objectives, methodological approaches, providing computational resources, editing, and review of the manuscript. K.B.D., E.O., and J.P. helped with data visualization and manuscript editing. R.B., P.M., L.U.A., J.M.-C., and Y.L. were involved in funding acquisition, manuscript review, and overall supervision. All authors contributed to the discussion and conceptualization of the study.

14 Competing Interests Statement

The authors declare no competing interests.

References

[1] Payette, S., Fortin, M.-J., Gamache, I.: The subarctic forest–tundra: the structure of a biome in a changing climate: the shifting of local subarctic tree lines throughout the forest–tundra biome, which is linked to ecological processes at different spatiotemporal scales, will reflect future global changes in climate. BioScience **51**(9), 709–718 (2001)

[2] Payette, S., Delwaide, A.: Tamm review: the north-american lichen woodland. Forest Ecology and Management **417**, 167–183 (2018)

[3] Montesano, P.M., Neigh, C., Sun, G., Duncanson, L., Van Den Hoek, J., Ranson, K.J.: The use of sun elevation angle for stereogrammetric boreal forest height in open canopies. Remote sensing of environment **196**, 76–88 (2017)

[4] St-Onge, B., Grandin, S.: Estimating the height and basal area at individual tree and plot levels in canadian subarctic lichen woodlands using stereo worldview-3 images. Remote Sensing **11**(3), 248 (2019)

[5] Government of Canada, S.C.: Terrestrial Ecozones and Ecoprovinces of Canada. https://www.statcan.gc.ca/en/subjects/standard/environment/elc/2017-map (2018)

[6] Ecological Stratification Working Group (Canada): A National Ecological Framework for Canada. Centre for Land and Biological Resources Research and Environment Canada, State of the Environment Directorate, Hull, Quebec (1996)

[7] Hermosilla, T., Wulder, M.A., White, J.C., Coops, N.C.: Land cover classification in an era of big and open data: Optimizing localized implementation and training data selection to improve mapping outcomes. Remote Sensing of Environment **268**, 112780 (2022)

[8] Rowe, J.S.: Forest regions of canada. Canadian Forestry Service **1300**, 172 (1972)

[9] Timoney, K., La Roi, G., Zoltai, S., Robinson, A.: The high subarctic forest-tundra of northwestern canada: position, width, and vegetation gradients in relation to climate. Arctic, 1–9 (1992)

[10] Sulla-Menashe, D., Friedl, M.A., Woodcock, C.E.: Sources of bias and variability in long-term landsat time series over canadian boreal forests. Remote Sensing of Environment **177**, 206–219 (2016)

[11] Sulla-Menashe, D., Woodcock, C.E., Friedl, M.A.: Canadian boreal forest greening and browning trends: an analysis of biogeographic patterns and the relative roles of disturbance versus climate drivers. Environmental Research Letters **13**(1), 014007 (2018)

[12] Ju, J., Masek, J.G.: The vegetation greenness trend in canada and us alaska from 1984–2012 landsat data. Remote Sensing of Environment **176**, 1–16 (2016)

[13] Griffiths, P., Linden, S., Kuemmerle, T., Hostert, P.: A pixel-based landsat compositing algorithm for large area land cover mapping. IEEE Journal of Selected Topics in Applied Earth Observations and Remote Sensing **6**(5), 2088–2101 (2013)

[14] White, J.C., Wulder, M., Hobart, G., Luther, J., Hermosilla, T., Griffiths, P., Coops, N., Hall, R., Hostert, P., Dyk, A., *et al.*: Pixel-based image compositing for large-area dense time series applications and science. Canadian Journal of Remote Sensing **40**(3), 192–212 (2014)

[15] Rouse Jr, J., Haas, R., Schell, J., Deering, D.: Paper a 20. In: Third Earth Resources Technology Satellite-1 Symposium: The Proceedings of a Symposium Held by Goddard Space Flight Center at Washington, DC On, vol. 351, p. 309 (1973)

[16] Bastiaanssen, W.G., Menenti, M., Feddes, R., Holtslag, A.: A remote sensing surface energy balance algorithm for land (sebal). 1. formulation. Journal of hydrology **212**, 198–212 (1998)

[17] Shamloo, N., Taghi Sattari, M., Apaydin, H., Valizadeh Kamran, K., Prasad, R.: Evapotranspiration estimation using sebal algorithm integrated with remote sensing and experimental methods. International Journal of Digital Earth **14**(11), 1638–1658 (2021)

[18] Verdonen, M., Berner, L.T., Forbes, B.C., Kumpula, T.: Periglacial vegetation dynamics in arctic russia: decadal analysis of tundra regeneration on landslides with time series satellite imagery. Environmental research letters **15**(10), 105020 (2020)

[19] Frank, A., Karn, J.: Vegetation indices, co2 flux, and biomass for northern plains grasslands. Rangeland Ecology & Management/Journal of Range Management Archives **56**(4), 382–387 (2003)

[20] Bezerra, B.G., Silva, B.B., Santos, C.A., Bezerra, J.R.: Actual evapotranspiration estimation using remote sensing: comparison of sebal and sseb approaches. Advances in Remote Sensing **4**(3), 234–247 (2015)

[21] Verhoeven, V.B., Dedoussi, I.C.: Annual satellite-based ndvi-derived land cover of europe for 2001–2019. Journal of Environmental Management **302**, 113917 (2022) https://doi.org/10.1016/j.jenvman.2021.113917

[22] Wang, Q., Moreno-Martínez, Á., Muñoz-Marí, J., Campos-Taberner, M., Camps-Valls, G.: Estimation of vegetation traits with kernel ndvi. ISPRS Journal of Photogrammetry and Remote Sensing **195**, 408–417 (2023)

[23] Miura, T., Nagai, S., Takeuchi, M., Ichii, K., Yoshioka, H.: Improved characterisation of vegetation and land surface seasonal dynamics in central japan with himawari-8 hypertemporal data. Scientific Reports **9**(1), 15692 (2019)

[24] Fang, J., Li, X., Xiao, J., Yan, X., Li, B., Liu, F.: Vegetation photosynthetic phenology dataset in northern terrestrial ecosystems. Scientific Data **10**(1), 300 (2023)

[25] Montaldo, N., Gaspa, A., Corona, R.: Assimilation of ndvi data in a land surface–vegetation model for leaf area index predictions in a tree-grass ecosystem. International Journal of Digital Earth **16**(1), 3810–3837 (2023)

[26] Holben, B.N.: Characteristics of maximum-value composite images from temporal avhrr data. International journal of remote sensing **7**(11), 1417–1434 (1986)

[27] Zaitunah, A., Samsuri, Ahmad, A., Safitri, R.: Normalized difference vegetation index (ndvi) analysis for land cover types using landsat 8 oli in besitang watershed, indonesia. In: IOP Conference Series: Earth and Environmental Science, vol. 126, p. 012112 (2018). IOP Publishing

[28] U.S. Geological Survey: NDVI, the Foundation for Remote Sensing Phenology. https://www.usgs.gov/special-topics/remote-sensing-phenology/science/ndvi-foundation-remote-sensing-phenology. Accessed: 2025-06-28 (2018)

[29] Myers-Smith, I.H., Kerby, J.T., Phoenix, G.K., Bjerke, J.W., Epstein, H.E., Assmann, J.J., John, C., Andreu-Hayles, L., Angers-Blondin, S., Beck, P.S., *et al.*: Complexity revealed in the greening of the arctic. Nature Climate Change **10**(2), 106–117 (2020)

[30] Wang, J.A., Friedl, M.A.: The role of land cover change in arctic-boreal greening and browning trends. Environmental Research Letters **14**(12), 125007 (2019)

[31] Berner, L.T., Goetz, S.J.: Satellite observations document trends consistent with a boreal forest biome shift. Global change biology **28**(10), 3275–3292 (2022)

[32] Nill, L., Grünberg, I., Ullmann, T., Gessner, M., Boike, J., Hostert, P.: Arctic shrub expansion revealed by landsat-derived multitemporal vegetation cover fractions in the western canadian arctic. Remote Sensing of Environment **281**, 113228 (2022) https://doi.org/10.1016/j.rse.2022.113228

[33] Pattison, R.R., Jorgenson, J.C., Raynolds, M.K., Welker, J.M.: Trends in ndvi and tundra community composition in the arctic of ne alaska between 1984 and 2009. Ecosystems **18**(4), 707–719 (2015)

[34] Fraser, R., Olthof, I., Carrière, M., Deschamps, A., Pouliot, D.: A method for trend-based change analysis in arctic tundra using the 25-year landsat archive. Polar record **48**(1), 83–93 (2012)

[35] Frost, G.V., Epstein, H.E., Walker, D.A.: Regional and landscape-scale variability of landsat-observed vegetation dynamics in northwest siberian tundra. Environmental Research Letters **9**(2), 025004 (2014)

[36] Raynolds, M.K., Walker, D.A., Verbyla, D., Munger, C.A.: Patterns of change within a tundra landscape: 22-year landsat ndvi trends in an area of the northern foothills of the brooks range, alaska. Arctic, antarctic, and alpine research **45**(2), 249–260 (2013)

[37] Guay, K.C., Beck, P.S., Berner, L.T., Goetz, S.J., Baccini, A., Buermann, W.: Vegetation productivity patterns at high northern latitudes: A multi-sensor satellite data assessment. Global change biology **20**(10), 3147–3158 (2014)

[38] Hermosilla, T., Wulder, M.A., White, J.C., Coops, N.C.: Land cover classification in an era of big and open data: Optimizing localized implementation and training data selection to improve mapping outcomes. Remote Sensing of Environment **268**, 112780 (2022)

[39] Zhang, X., Zhao, T., Xu, H., Liu, W., Wang, J., Chen, X., Liu, L.: Glc_fcs30d: The first global 30-m land-cover dynamic monitoring product with a fine classification system from 1985 to 2022 using dense time-series landsat imagery and continuous change-detection method. Earth System Science Data Discussions **2023**, 1–32 (2023)